

3DGEER: Exact and Efficient Volumetric Rendering with 3D Gaussians

ZIXUN HUANG, CHO-YING WU, YULIANG GUO[†], XINYU HUANG, LIU REN

Bosch Research North America & Bosch Center for AI

<https://zixunh.github.io/3d-geer>

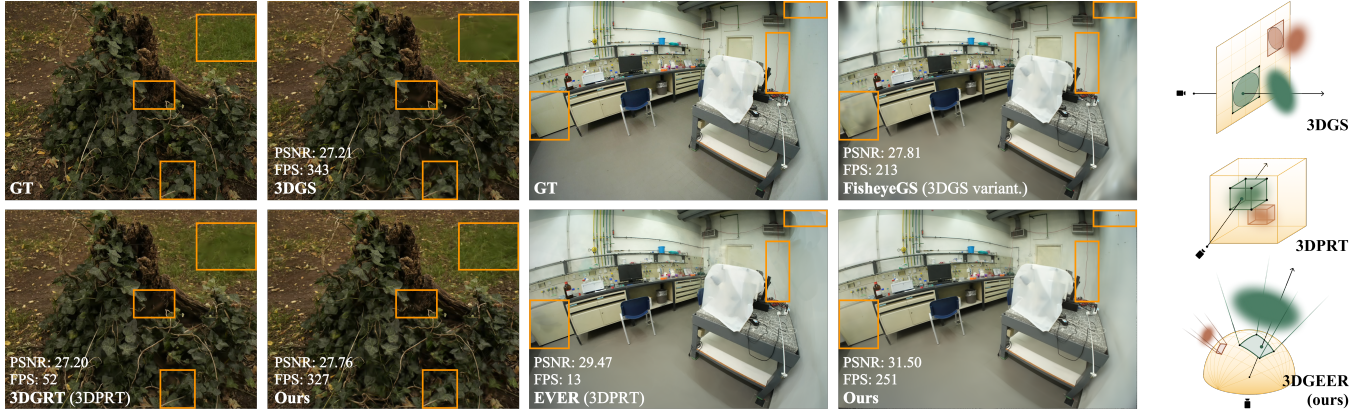


Fig. 1. **An Overview of 3DGEER's Performance Advantages and Technical Innovations.** 3DGEER, an exact and efficient volumetric Gaussian rendering method, outperforms both 3DGS-based (Gaussian Splatting) and 3DPRT-based (Particle Ray Tracing) methods on novel view synthesis benchmarks under (Left) MipNeRF360 (pinhole) and (Middle) ScanNet++ (fisheye), while maintaining high runtime efficiency. (Right) Leveraging a closed-form ray integral and tight frustum computation per Gaussian, 3DGEER eliminates projective approximations compared to 3DGS variants and surpasses 3DPRT methods significantly in speed. Here, 3DPRT refers to ray-tracing-based volumetric particle renderers, including 3DGRT (Gaussian) and EVER (ellipsoid).

3D Gaussian Splatting (3DGS) [Kerbl et al. 2023] marks a significant milestone in balancing the quality and efficiency of differentiable rendering. However, its high efficiency stems from an approximation of projecting 3D Gaussians onto the image plane as 2D Gaussians, which inherently limits rendering quality—particularly under large Field-of-View (FoV) camera inputs. While several recent works have extended 3DGS to mitigate these approximation errors, none have successfully achieved both exactness and high efficiency simultaneously. In this work, we introduce 3DGEER, an Exact and Efficient Volumetric Gaussian Rendering method. Starting from first principles, we derive a closed-form expression for the density integral along a ray traversing a 3D Gaussian distribution. This formulation enables precise forward rendering with arbitrary camera models and supports gradient-based optimization of 3D Gaussian parameters. To ensure both exactness and real-time performance, we propose an efficient method for computing a tight Particle Bounding Frustum (PBF) for each 3D Gaussian, enabling accurate and efficient ray-Gaussian association. We also introduce a novel Bipolar Equiangular Projection (BEAP) representation to accelerate ray association under generic camera models. BEAP further provides a more uniform ray sampling strategy to apply supervision, which empirically improves reconstruction quality. Experiments on multiple pinhole and fisheye datasets show that our method consistently outperforms prior methods, establishing a new state-of-the-art in real-time neural rendering.

CCS Concepts: • **Computing methodologies** → Rendering; Reconstruction; Machine Learning Approaches.

Additional Key Words and Phrases: Volumetric Rendering, Differentiable Rendering, Novel View Synthesis, Radiance Fields, Neural Reconstruction

1 INTRODUCTION

Initiated by 3D Gaussian Splatting (3DGS) [Kerbl et al. 2023], volumetric particle rendering methods formulated under splatting [Charatan et al. 2024; Kheradmand et al. 2024; Lu et al. 2024; Mallick

et al. 2024; Yan et al. 2024; Yu et al. 2024a] have gained significant popularity due to their impressive visual fidelity and high rendering speed. The core efficiency stems from EWA splatting [Zwicker et al. 2001], which uses a local affine approximation to project a 3D Gaussian as a 2D Gaussian on the image plane. While effective in narrow field-of-view (FoV) scenarios, this approximation introduces substantial errors in wide-FoV settings, where nonlinear distortions cause the true projection to deviate significantly from a symmetric 2D Gaussian—especially in fisheye images commonly encountered in robotics and autonomous driving [Courbon et al. 2007; Kumar et al. 2023; Rashed et al. 2021; Sekkat et al. 2022; Yogamani et al. 2019, 2024; Zhang et al. 2016]. Although recent works have attempted to enable differentiable rendering under specific fisheye camera models [Liao et al. 2024] or more general camera models [Huang et al. 2024], these approaches remain fundamentally constrained by their reliance on 2D projective-space approximations and have yet to yield an exact closed-form solution.

A parallel line of work tackles volumetric particle rendering directly in a ray-marching formulation [Condor et al. 2025; Mai et al. 2024; Moënné-Loccoz et al. 2024; Yu et al. 2024b]. These approaches naturally support large-FoV camera models and are free from projective approximation error. However, achieving high efficiency remains a key challenge—particularly in associating each rendering ray with its most relevant 3D particles. To address this, significant effort has been devoted to accelerating it, such as adopting advanced Bounding Volume Hierarchies (BVH) employed in EVER [Mai et al. 2024] and 3DGRT [Moënné-Loccoz et al. 2024]. Nevertheless, due to the inherent algorithmic complexity and difficulty in parallelization, pure ray marching methods have yet to match the efficiency of 3DGS. Alternatively, a hybrid approach has been proposed in

[†] Corresponding Author.

3DGUT [Wu et al. 2025] which adopts ray-tracing rendering with rasterization to solve ray-particle association efficiently. However, the inherited projective approximation error from association stage still compromises rendering exactness. To date, no existing method achieves both the exactness of ray-based rendering and the high efficiency of projection-based splatting.

In this work, we propose 3DGEER (3D Gaussian Exact and Efficient Rendering)—a novel volumetric Gaussian rendering method that achieves exact rendering while maintaining high efficiency comparable to 3DGS (see Fig. 1). 3DGEER is built upon three key technical contributions: (i) Instead of relying on projective approximations or 2D conic fitting, we revisit ray-marching-based volumetric Gaussian rendering from first principles and derive a closed-form solution for integrating density along a 3D ray through a Gaussian. Based on it, we further derive the exact volumetric Gaussian rendering framework. (ii) To perform efficient ray-particle association without compromising rendering exactness, we reformulate the problem as associating Camera Sub-frustums (CSF) with Particle Bounding Frustums (PBF)—analogous to the tile-AABB mapping used in 3DGS. For each 3D Gaussian, we derive a closed-form solution to compute the PBF tightly bounding it, enabling highly efficient association. (iii) In addition, we propose to uniformly sample rays in a novel Bipolar Equiangular Projection (BEAP) space to apply color supervision. This ray sampling strategy not only aligns image-space partitioning and the underlying CSF but also improved conventional pinhole or equidistant projections in reconstruction quality. Extensive experiments on both fisheye and pinhole datasets—including ScanNet++ [Yeshwanth et al. 2023], Zip-NeRF [Barron et al. 2023], and MipNeRF [Barron et al. 2021]—show that 3DGEER consistently outperforms prior and concurrent methods, achieving 0.9–4.8 PSNR gains under challenging wide-FoV conditions, and 0.3–2.0 on pinhole views.

In summary, our contributions are as follows:

- (1) We present the first complete, first-principle derived, closed-form solution for exact volumetric Gaussian rendering;
- (2) We propose an exact and efficient ray-particle association method that enables high speed rendering;
- (3) We introduce an equiangular ray sampling strategy that provides more spatially uniform color supervision.
- (4) Our method consistently outperforms SOTA approaches across multiple datasets, with notable gains on wide-FoV neural reconstruction benchmarks.

2 RELATED WORKS

2.1 Splatting-Based Gaussian Rendering

Most 3DGS variants [Charatan et al. 2024; Chen et al. 2024a,b; Cheng et al. 2024; Chung et al. 2024; Guédon and Lepetit 2024; Kerbl et al. 2024; Kheradmand et al. 2024; Lee et al. 2024a,b; Lu et al. 2024; Mallick et al. 2024; Rota Bulò et al. 2024; Yan et al. 2024; Yu et al. 2024a; Zhang et al. 2024] adopt the original EWA splatting [Zwicker et al. 2001] strategy, projecting 3D Gaussians onto the image plane and approximating their appearance as 2D conics. To support differentiable rendering under large-FoV camera models with distortion, methods such as FisheyeGS [Liao et al. 2024] and GS++ [Huang et al. 2024] estimate the Jacobian of equidistant or spherical projections to adjust the 2D mean and covariance of the projected Gaussians.

Table 1. **Summary of Volumetric Particle Rendering Methods wrt. Exactness.** The top section lists splatting-based methods, while the bottom section presents ray-marching-based approaches—some of which still rely on projective approximations (e.g., EWA or Unscented Transform) during ray-particle association.

Method	Render	Particle Asso.		Particle Type	Large FoV	High FPS	Exact Meth.
		Meth.	Scope				
3DGS [2023]	Splat.	EWA	Img.	3D Gauss.	✗	✓	✗
FisheyeGS [2024]	Splat.	EWA	Img.	3D Gauss.	✓	✓	✗
GS++ [2024]	Splat.	EWA	Img.	3D Gauss.	✗	✓	✗
GOF [2024b]	Ray	EWA	Img.	3D Gauss.	✗	✗	✗
EVER [2024]	Ray	BVH	Scene	3D Ellip.	✓	✗	✓
3DGRT [2024]	Ray	BVH	Scene	3D Gauss.	✓	✗	✓
3DGUT [2025]	Ray	UT	Img.	3D Gauss.	✓	✓	✗
3DGEER (Ours)	Ray	PBF	Frust.	3D Gauss.	✓	✓	✓

However, these splatting-based approaches still rely on a first-order Taylor expansion of the highly non-linear projection function. In wide-FoV settings, higher-order terms is non-negligible, resulting in significant approximation errors and degraded reconstruction quality.

Fundamentally, the true projection of a 3D Gaussian under non-linear camera models—whether ideal pinhole or distorted projections—is not a symmetric 2D Gaussian. In other words, any framework that relies on linear projective geometry to approximate inherently nonlinear transformations will inevitably introduce approximation errors that cannot be fully eliminated. In contrast, our approach avoids such projective approximations entirely by aggregating Gaussian density directly along rays in a volumetric rendering formulation.

2.2 Ray-Marching-Based Gaussian Rendering

A few recent works have approached volumetric particle rendering using a ray-marching formulation, which inherently supports arbitrary camera models without introducing projective approximation error. 3DGRT [Moenne-Loccoz et al. 2024], inspired by fuzzy metaball rendering [Keselman and Hebert 2022], approximates the ray-Gaussian interaction as the location of maximum intensity response. This heuristic enables ray-space sampling without explicit projection, effectively mitigating wide-FoV distortion. However, it incurs significant computational overhead due to the high cost of ray-particle association via scene-level spatial partitioning structures such as BVH, ultimately resulting in low frame rates.

Alternatively, EVER [Mai et al. 2024] replaces the Gaussian representation with simplified ellipsoids of constant density, enabling a closed-form solution for transmittance-weighted ray integration. However, it reduces the expressive capacity of the representation compared to full 3D Gaussians, and continues to suffer from low runtime efficiency due to its reliance on BVH-based structures.

3DGUT [Wu et al. 2025], a follow-up to 3DGRT, improves runtime efficiency by adopting splatting-based particle association, achieving frame rates comparable to 3DGS. However, its acceleration relies on the Unscented Transform (UT), a sampling-based approximation used to estimate 2D conics in projective image space. While the rendering stage is ray-based, the ray-particle association still

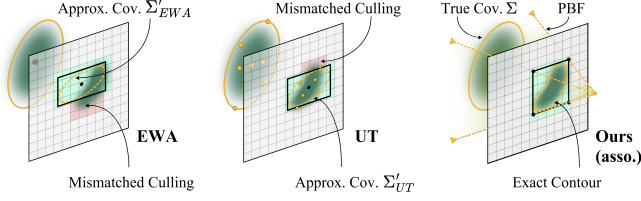


Fig. 2. **Projective Approximation Error in Ray-Particle Association.** When projecting a Gaussian particle from 3D space onto the image plane, both EWA and Unscented Transform (UT)-based association methods approximate the 2D covariance of the projection. They then either tighten the bounding box—risking mismatched culling—or overestimate it using the maximum projected radius of the conic. In contrast, our PBF method avoids this intermediate approximation by directly computing the exact bounding structure from the true 3D covariance.

introduces approximation errors akin to those in EWA splatting. A similar limitation exists in GOF [Yu et al. 2024b], which directly applies the EWA trick to fit 2D bounding conics and projective centers for association. Notably, under extreme FoV conditions, imprecise AABB estimation and the resulting inaccurate tile-to-AABB associations can lead to visible rendering artifacts (see Figure 2).

In contrast to these methods, our approach solves the ray-particle association problem directly at the frustum level in 3D space, preserving the exactness of ray-based rendering across arbitrary camera models while maintaining rendering speeds comparable to 3DGS. Table 1 summarizes representative methods that aim to address projective approximation errors, highlighting key differences across several important dimensions.

3 3DGEER

Our method, 3DGEER, is built upon three key components: an exact ray-based volumetric Gaussian rendering formulation, an efficient frustum-particle association strategy, and an effective image representation. In Sec.3.1, we introduce the necessary preliminaries. Sec.3.2 presents the closed-form solution for Gaussian density integral along a 3D ray, followed by our differentiable volumetric rendering method that supports arbitrary FoV camera models. In Sec.3.3, we propose a novel and efficient approach for ray-particle association based on fast, exact computation of the Particle Bounding Frustum (PBF). Finally, in Sec.3.4, we detail the Bipolar Equiangular Projection (BEAP) image representation, which seamlessly supports generic camera models and accelerates frustum-particle association while improving reconstruction quality in practice.

3.1 Preliminaries

We follow the classic parameterization of 3D Gaussian primitives as introduced in prior work [Zwicker et al. 2001]. Each 3D Gaussian distribution is defined by a mean position $\mu \in \mathbb{R}^3$ and a 3D covariance matrix Σ in the world coordinate system:

$$\mathcal{G}_{\Sigma, \mu}(\mathbf{x}) = \frac{1}{\rho |\Sigma|^{1/2}} \exp\left(-\frac{1}{2}(\mathbf{x} - \mu)^\top \Sigma^{-1}(\mathbf{x} - \mu)\right), \quad (1)$$

where we adopt the normalization constant ρ as $\sqrt{2\pi}$, and $\mathbf{x} \in \mathbb{R}^3$ denotes a point in world space. This formulation differs from recent methods such as 3DGS [Kerbl et al. 2023] and 3DGUT [Wu et al. 2025], which omit the determinant term $|\Sigma|^{1/2}$ to simplify splatting

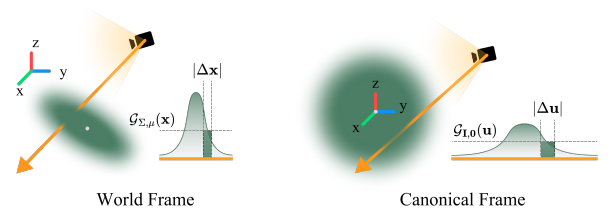


Fig. 3. **Integral of 3D Gaussian Density along a Ray.** Under the transformation from the world frame to the canonical frame, the ray integral remains invariant. The green box highlights the product of density and ray segment length (see Eq. 5).

or association during rendering. The form of our covariance matrix obeys: $\Sigma = RSS^\top R^\top$, given a scaling matrix $S = \text{diag}(\mathbf{s})$ constructed from the scaling vector $\mathbf{s} \in \mathbb{R}^3$, and a rotation matrix $R \in \text{SO}(3)$ derived from a unit quaternion $\mathbf{q} \in \mathbb{R}^4$.

To evaluate the transmittance contributed by a single 3D Gaussian particle along a ray $\mathbf{r}(t) = \mathbf{o} + t\mathbf{d}$, we have:

$$T(\mathbf{o}, \mathbf{d}) = \sigma \int_{t \in \mathbb{R}} \mathcal{G}_{\Sigma, \mu}(\mathbf{o} + t\mathbf{d}) dt, \quad (2)$$

where σ is the opacity coefficient associated with the Gaussian.

Finally, considering a set of 3D Gaussian particles sorted by depth contributing to the rendering color of the given ray, the rendered color C is computed as:

$$C(\mathbf{o}, \mathbf{d}) = \sum_i c_i(\mathbf{o}, \mu_i) T_i \prod_{j=1}^{i-1} (1 - T_j), \quad (3)$$

where $c_i(\mathbf{o}, \mu_i)$ derives the view-dependent color of the i -th Gaussian as seen from the optical center \mathbf{o} , parameterized using spherical harmonics (SH) [Kerbl et al. 2023]. Through minimizing the reconstruction loss between the rendered color and the observed color along each ray, the parameters $\mathbf{s}, \mathbf{q}, \mu$, the coefficient σ as well as the SH coefficients, are jointly optimized via backpropagation.

3.2 Exact Volumetric Gaussian Rendering

The core challenge in achieving exact volumetric Gaussian rendering in a ray marching formulation lies in obtaining a closed-form solution for integrating Gaussian density and color along a 3D ray. To address this, we first transform the ray—relative to each Gaussian—into a canonical coordinate system where the transmittance integral (see Eq. B.4) remains consistent and the Gaussians become isotropic. We then derive the exact ray color from first principles.

Specifically, we define a canonical coordinate system shared across all 3D Gaussian primitives. A point $\mathbf{u} \in \mathbb{R}^3$ in this canonical space is mapped to world coordinates for each Gaussian via:

$$\begin{bmatrix} \mathbf{x} \\ 1 \end{bmatrix} = H \begin{bmatrix} \mathbf{u} \\ 1 \end{bmatrix} = \begin{bmatrix} RS & \mu \\ \mathbf{0} & 1 \end{bmatrix} \begin{bmatrix} \mathbf{u} \\ 1 \end{bmatrix}, \quad (4)$$

From this transformation, an infinitesimal segment $\Delta \mathbf{u}$ along a ray in the canonical frame corresponds to a segment $\Delta \mathbf{x} = RS\Delta \mathbf{u}$ in the world frame.

To ensure that the transmittance contributed by each Gaussian along the ray is preserved across coordinate systems, we require that the elementary transmittance (i.e., the product of density and

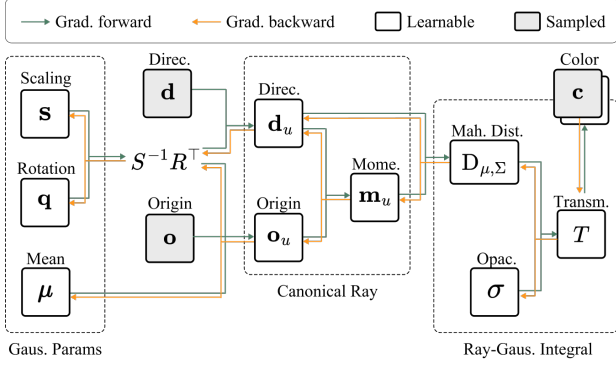


Fig. 4. **Pipeline Flowchart.** Illustration of forward and backward gradient propagation from the Gaussian parameters \mathbf{s} , \mathbf{q} , $\boldsymbol{\mu}$, and the coefficient σ to the transmittance.

segment length) remains invariant under the transformation (see Figure 3):

$$\mathcal{G}_{\mathbf{I},0}(\mathbf{u}) |\Delta \mathbf{u}| = \mathcal{G}_{\Sigma,\boldsymbol{\mu}}(\mathbf{x}) |\Delta \mathbf{x}|. \quad (5)$$

This constraint implies that the Jacobian determinant is absorbed into the measure. Note that $|\frac{\Delta \mathbf{x}}{\Delta \mathbf{u}}| = |\mathbf{R}\mathbf{S}| = |\Sigma|^{1/2}$. We can thus express the corresponding canonical density as:

$$\mathcal{G}_{\mathbf{I},0}(\mathbf{u}) = \frac{1}{\rho} \exp\left(-\frac{1}{2} \mathbf{u}^\top \mathbf{u}\right), \quad (6)$$

which is isotropic and shared across all primitives in canonical space.

This leads to an important conclusion that the exact closed-form solution for the transmittance integral of each Gaussian along the ray $\mathbf{r}(t)$ can thus be obtained by computing the accumulated density along the transformed ray $\mathbf{r}_u(t) = \mathbf{o}_u + t\mathbf{d}_u$ in the canonical isotropic Gaussian. This admits a *closed-form* solution in terms of the perpendicular distance from the ray to the Gaussian center, as captured in Theorem B.1. (see Appendix B for a complete proof):

$$T(\mathbf{o}, \mathbf{d}) = \sigma \int_{t \in \mathbb{R}} \mathcal{G}_{\mathbf{I},0}(\mathbf{o}_u + t\mathbf{d}_u) dt = \sigma \exp\left(-\frac{1}{2} (D_{\mu,\Sigma}(\mathbf{o}, \mathbf{d}))^2\right), \quad (7)$$

where $D_{\mu,\Sigma}(\mathbf{o}, \mathbf{d})$ denotes the perpendicular distance from the Gaussian center (i.e., the origin in the canonical space) to the transformed ray $\mathbf{r}_u(t)$. Intuitively, this quantity also represents the minimal *Ma-halanobis distance* from any points on the ray to the Gaussian in world space, measuring how close the ray passes by the particle distribution.

The remaining question is just about how to compute the perpendicular distance from the canonical origin to the transformed ray. We derive the transformed ray’s direction vector \mathbf{d}_u and moment vector \mathbf{m}_u as:

$$\mathbf{d}_u = (S^{-1}R^\top) \mathbf{d}, \quad \mathbf{m}_u = \mathbf{o}_u \times \mathbf{d}_u, \quad (8)$$

where $\mathbf{o}_u = (S^{-1}R^\top) (\mathbf{o} - \boldsymbol{\mu})$ denotes the optical center in canonical space. Based on this, the square of $D_{\mu,\Sigma}(\mathbf{o}, \mathbf{d})$ can be efficiently calculated as:

$$(D_{\mu,\Sigma}(\mathbf{o}, \mathbf{d}))^2 = \frac{\mathbf{m}_u^\top \mathbf{m}_u}{\mathbf{d}_u^\top \mathbf{d}_u}. \quad (9)$$

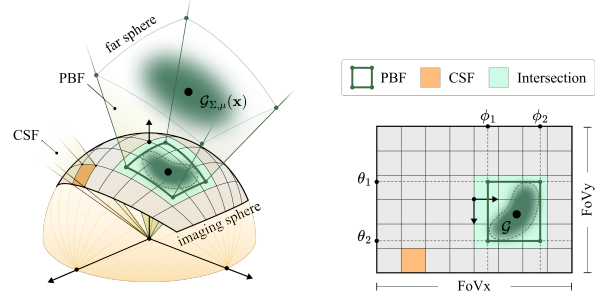


Fig. 5. **An Illustration of PBF-CSF Association.** *Left:* Each PBF and CSF is parameterized by four spherical angles, with the PBF additionally defined by four planes tangent to a 3D Gaussian ellipsoid. *Right:* The intersection between the PBF and CSF, unfolded onto the BEAP imaging plane.

By substituting this distance square into Eq. 7, and then the derived transmittance value into Eq. 3, we compute the accumulated color along the ray.

To minimize the computational overhead caused by automatic differentiation during training, we explicitly derive the ray-integral function and the gradients from the transmittance to all the Gaussian parameters, specifically $\frac{\partial T}{\partial \mathbf{s}}$, $\frac{\partial T}{\partial \mathbf{q}}$, $\frac{\partial T}{\partial \boldsymbol{\mu}}$. The detailed derivations for these derivatives are provided in Appendix C and visually explained in the Figure 4.

3.3 Efficient Ray-Particle Association via PBF

Given an exact volumetric Gaussian rendering method, both its final accuracy—particularly under large FoV camera models—and its runtime efficiency depend heavily on the ray-particle association strategy. To determine which Gaussians contribute to each ray, we simplify the association problem by mapping Camera CSFs to PBFs—the tight frustums enclosing each Gaussian at a certain distance from its center. A Gaussian is assigned to a CSF if its PBF intersects the CSF. All Gaussians associated with a CSF are then considered contributors to every ray within that CSF.

To efficiently compute a PBF, we first define two spherical angles (See Fig. A.1 in Appendix A) in the camera space as:

$$\theta = \arctan\left(\frac{\mathbf{d}_{c,x}}{\mathbf{d}_{c,z}}\right), \quad \phi = \arctan\left(\frac{\mathbf{d}_{c,y}}{\mathbf{d}_{c,z}}\right), \quad (10)$$

where $(\mathbf{d}_{c,x}, \mathbf{d}_{c,y}, \mathbf{d}_{c,z})$ denotes the normalized direction vector pointing to the camera (view) space point \mathbf{d}_c . The angles θ and ϕ correspond to the ray’s incidence angles in the horizontal (xz) and vertical (yz) planes, respectively, each ranging from $-\frac{\pi}{2}$ to $\frac{\pi}{2}$.

We define a PBF by four planes — two aligned with the θ angle and two with the ϕ angle (See Figure 5):

$$\mathbf{g}_{\theta_{1,2}} = (-1, 0, \tan \theta_{1,2}, 0)^\top, \quad \mathbf{g}_{\phi_{1,2}} = (0, -1, \tan \phi_{1,2}, 0)^\top, \quad (11)$$

where $\theta_1 < \theta < \theta_2$ and $\phi_1 < \phi < \phi_2$ specify the angular limits.

Given a camera with extrinsic matrix $V = [\mathbf{R}_c | \mathbf{t}_c] \in \text{SE}(3)$ and a canonical-to-world transformation matrix H (See Eq. 4), we apply the inverse transpose of the camera-to-canonical matrix $(VH)^{-1}$ to parameterize the corresponding canonical planes using the angular limits defined in view space. This transformation enables us to effectively derive the constraints for the PBFs. The canonical planes

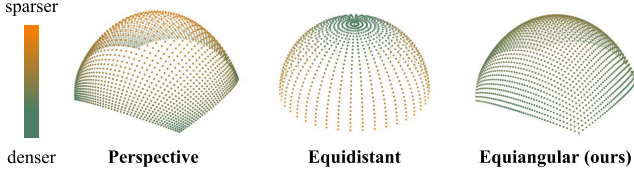


Fig. 6. **Comparison of Ray Distributions under Varying Projections.** Each point represents a sampled ray, defined by the intersection between a ray from the optical center and the sphere surface. Our BEAP projection yields the most uniform ray distribution across the sphere surface.

are given by:

$$\begin{aligned} \mathbf{g}_{u,1,2} &= (VH)^\top \mathbf{g}_{\theta_{1,2}} = -(VH)_0 + \tan \theta_{1,2} (VH)_2, \\ \mathbf{g}_{\phi_{1,2}} &= (VH)^\top \mathbf{g}_{\phi_{1,2}} = -(VH)_1 + \tan \phi_{1,2} (VH)_2, \end{aligned} \quad (12)$$

where $(VH)_i$ denotes the i -th row of the matrix, expressed as a column vector.

Assuming a Gaussian ellipsoid defined by a λ -standard-deviation contour, we compute the angular bounds of the local frustum by solving the following quadratic equations, which enforce that the transformed planes are tangent to the ellipsoidal contour:

$$\left((\lambda^2, \lambda^2, \lambda^2, -1) \circ \mathbf{g}_u^\top \right) \cdot \mathbf{g}_u = 0, \quad (13)$$

where \circ denotes the Hadamard (element-wise) product, and λ is a parameter that controls the spread of the contour, typically set to 3. An identical constraint is applied to \mathbf{g}_v^\top in order to compute the corresponding angular bounds $\phi_{1,2}$.

The roots of these quadratic equations determine the tangent values of the angular bounds $[\theta_1, \theta_2]$ and $[\phi_1, \phi_2]$, which define the PBF angular limits. Notably, solving these quadratic equations under canonical space constraints respects the true 3D covariance and 3D mean of the Gaussian. This formulation is both efficient and eliminates the need for any intermediate approximation steps as adopted in EWA or UT (See Appendix E.1 for details).

3.4 Bipolar Equiangular Projection (BEAP)

We introduce a novel BEAP image representation for several reasons. First, it effectively represents images from large field-of-view (FoV) cameras without introducing FoV loss. Second, it allows image tiles and their corresponding Camera Sub-frustums (CSFs) to share an identical parameterization in terms of two θ and two ϕ angles, enabling highly efficient PBF association and optimal GPU parallelization. Third, the resulting ray sampling achieves a more uniform distribution in 3D space compared to conventional projective rendering, which empirically improves training efficiency and reconstruction quality, as shown in the ablation study in Sec. 5.2.

Specifically, we evenly sample the rays using the spherical angular coordinates (θ, ϕ) (See Eq. 10), and then map the rays back to a discrete $w \times h$ image space using a linear transformation consisting of a scaling factor and a center shift as:

$$(x, y) = \left\lfloor \frac{w\theta}{\text{FoV}_x} + \frac{w+1}{2}, \frac{h\phi}{\text{FoV}_y} + \frac{h+1}{2} \right\rfloor, \quad (14)$$

where FoV_x , FoV_y indicate the camera’s horizontal and vertical field-of-view. As illustrated in Figure 6, sampling rays uniformly in (θ, ϕ)

Table 2. **Quantitative Results on the ScanNet++ Dataset.** Each method is trained using full FoV data but evaluated separately on the full FoV, central, and peripheral regions to assess performance under varying distortion levels. The region-wise metrics is weighted by pixel-wise masks, where LPIPS is omitted as it is not directly separable by region.

Method	Full FoV			Central		Peripheral	
	PSNR \uparrow	SSIM \uparrow	LPIPS \downarrow	PSNR \uparrow	SSIM \uparrow	PSNR \uparrow	SSIM \uparrow
FisheyeGS	27.81	0.946	0.139	32.44	0.956	23.28	0.914
EVER	29.47	0.924	0.167	29.93	0.924	28.72	0.925
3DGUT	30.64	0.944	0.150	31.87	0.945	28.84	0.937
3DGEER (Ours)	31.50	0.953	0.126	32.64	0.955	28.94	0.945

leads to more balanced spatial coverage within the view frustum. Our sampling strategy contrasts with projective sampling, which disproportionately allocates samples toward peripheral regions, and equidistant projection, which oversamples near the image center.

4 EXPERIMENTS

In this section, we evaluate our proposed method, 3DGEER, across multiple datasets featuring both pinhole and fisheye camera models.

Baselines. We compare 3DGEER with leading volumetric particle rendering methods targeting projective approximation errors in 3DGS [Kerbl et al. 2023]. For large FoV fisheye inputs, we evaluate against FisheyeGS [Liao et al. 2024], EVER [Mai et al. 2024], and 3DGUT [Wu et al. 2025]. Under pinhole settings, we additionally compare with 3DGS and 3DGRT [Moënne-Loccoz et al. 2024].

Datasets. To systematically evaluate performance under large FoV conditions, where projective approximation errors are most critical. We use five diverse scenes from the ScanNet++ [Yeshwanth et al. 2023] dataset and the fisheye ZipNeRF [Barron et al. 2023], which has been largely overlooked in prior work. For conventional pinhole settings, we use the standard ZipNeRF and the widely adopted MipNeRF360 [Barron et al. 2021] datasets.

Evaluation Metrics and Protocol. We report PSNR \uparrow , SSIM \uparrow , and LPIPS \downarrow to evaluate reconstruction and novel view synthesis quality, and runtime performance (FPS) to assess efficiency. To ensure fair comparison across methods with different internal representations, all outputs are projected back to the original image space before evaluation. This avoids representation bias and ensures full-FoV coverage. All methods are compared after 30k training iterations.

Implementation Details. To ensure fair comparison, we align our implementation with the original 3DGS in terms of initialization and hyperparameters on the ScanNet++ and MipNeRF360 datasets. For ZipNeRF, we adopt the training configurations of EVER and SMERF [Duckworth et al. 2024] for all candidate methods. Similar to most ray-based frameworks, our method does not directly access gradients of mean2D to control densification or pruning. Instead, we optimize using gradients of the view-space mean3D. Unless otherwise noted, all models are trained with consistent supervision strategies and architectural settings. For fisheye datasets (ScanNet++ and ZipNeRF), we precompute bijective grid mappings [Guo et al. 2025] and reproject all rendered outputs to the native KB-Fisheye image space [Kannala and Brandt 2006] before evaluation. Experiments on ScanNet++ and MipNeRF360 are conducted using full-resolution images. For ZipNeRF, due to the high frame count and extremely

Table 3. **Quantitative Results on the ZipNeRF Dataset.** The experiments follow a cross-camera generalization setup, where each method is trained on either Fisheye (FE) or Pinhole (PH) data and evaluated separately on both Fisheye and Pinhole test sets.

Train Data	1/8 FE		1/8 FE		1/8 FE		1/4 PH		1/4 PH		1/4 PH	
Test Data	1/8 FE	1/4 PH	1/8 FE	1/4 PH	1/8 FE	1/4 PH	1/8 FE	1/4 PH	1/8 FE	1/4 PH	1/8 FE	1/4 PH
Method	PSNR \uparrow		SSIM \uparrow		LPIPS \downarrow		PSNR \uparrow		SSIM \uparrow		LPIPS \downarrow	
FisheyeGS	23.18	26.44	0.858	0.868	0.211	0.239	19.43	26.61	0.791	0.889	0.247	0.212
EVER	25.17	26.14	0.880	0.851	0.153	0.237	22.90	26.45	0.835	0.862	0.207	0.222
3DGUT	24.77	25.59	0.879	0.804	0.183	0.324	18.61	25.96	0.662	0.841	0.300	0.270
3DGEER (Ours)	26.24	27.62	0.897	0.888	0.140	0.214	23.39	27.61	0.846	0.863	0.209	0.254

Table 4. **Quantitative Results on the MipNeRF360 Dataset.** In addition to quality metrics, FPS is reported using an RTX 4090 as the default benchmark. Numbers sourced from original works are marked with \ddagger (measured on RTX 6000 Ada) and $\hat{\dagger}$ (measured on RTX 5090).

Method	PSNR \uparrow	SSIM \uparrow	LPIPS \downarrow	FPS \uparrow
3DGS	27.21	0.815	0.214	343
EVER	27.51	0.825	0.233	36
3DGRT	27.20	0.818	0.248	52 $\hat{\dagger}$ / 68 \ddagger
3DGUT	27.26	0.810	0.218	265 $\hat{\dagger}$ / 317 \ddagger
3DGEER (Ours)	27.76	0.821	0.210	327

large fisheye resolution, we use the maximum resolution (see Tab. 3) that allows all baselines to run reliably on a local desktop setup. Specifically, all experiments are conducted using an RTX 4090 GPU and 64GB of RAM as the default configuration.

4.1 Evaluation on Large-FoV Novel View Synthesis

We evaluate 3DGEER against representative baselines on two fish-eye datasets designed for benchmarking novel view synthesis. To ensure a more comprehensive evaluation, we incorporate additional analysis tailored to each dataset.

ScanNet++. As shown in Tab. 2, our method consistently outperforms all prior methods across all metrics, with clear margins. To further analyze each method’s performance under varying distortion, we separately evaluate reconstruction quality in the central and peripheral image regions (Detailed rule explained in Appendix G). As expected, FisheyeGS—while effective at enabling differentiable rendering for fisheye inputs—does not explicitly address projective approximation error. It performs well in the central region but degrades significantly in the periphery. Although all methods show some performance drop in peripheral areas, 3DGEER achieves the best results in both regions. Qualitatively, as illustrated in Fig. 7, 3DGEER delivers superior peripheral reconstruction compared to FisheyeGS, exhibits fewer artifacts and sharper details than EVER, and produces crisper object boundaries and textures—such as wires, keyboards, and wooden floors—when compared to 3DGUT.

ZipNeRF. Since the ZipNeRF dataset provides frame-wise aligned pinhole and fisheye datasets, we go beyond standard evaluation on the fisheye dataset by also conducting a *cross-camera generalization* evaluation—training on fisheye views and evaluating on pinhole, and vice versa—to further assess each method’s robustness and adaptability. As shown in Tab. 3, 3DGEER consistently outperforms all other methods across all metrics when trained on fisheye data,

Table 5. **Runtime Analysis vs. Other Methods.** 3DGEER is compared with efficient splatting-based methods on MipNeRF360 and ScanNet++, with a thorough comparison in stage-wise and total runtime.

Dataset	Method	Avg. Timings (ms) \downarrow				
		Prep.	Dup.	Sort	Render	Total
MipNeRF360	3DGS	0.32	0.27	0.65	1.40	2.92
	3DGEER (Ours)	0.37	0.17	0.27	2.10	3.06
ScanNet++	FisheyeGS	0.10	0.63	1.45	2.33	4.70
	3DGEER (Ours)	0.13	0.26	0.59	2.89	3.98

regardless of whether the test set is fisheye or pinhole. This highlights 3DGEER’s ability to fully leverage the advantages of large FoV training data through exact volumetric rendering. When training on pinhole data, 3DGEER also achieves significant PSNR improvements on both fisheye and pinhole test sets. In contrast, FisheyeGS performs well when both training and testing are done on pinhole images, but its performance drops sharply when evaluated on fisheye inputs. Similarly, 3DGUT exhibits a substantial decline when tested on fisheye views after training on narrower FoV data. Overall, EVER and 3DGEER demonstrate the most robust generalization across camera models—attributed to their preservation of geometric exactness—while 3DGEER consistently outperforms EVER across all scenarios. Qualitatively, as shown in Fig. 9, 3DGEER reconstructs finer details and exhibits greater robustness to artifacts than competing methods, both in challenging peripheral regions and cross-camera evaluation settings.

4.2 Evaluation on Normal-FoV Novel View Synthesis

We further evaluate 3DGEER on the **MipNeRF360** dataset to demonstrate its effectiveness under standard, narrow-FoV conditions. As shown in Tab. 4, 3DGEER achieves strong performance across all metrics, setting a new state-of-the-art. This evaluation also includes a runtime comparison in terms of FPS. Notably, 3DGEER is over 5 \times more efficient than other exact ray-marching methods such as EVER and 3DGRT, and is the only exact method with runtime comparable to the original 3DGS. Additionally, it consistently outperforms projective-approximation-based methods—including 3DGS and 3DGUT—in PSNR, SSIM, and LPIPS.

4.3 Comprehensive Runtime Analysis

We begin by analyzing runtime performance, comparing 3DGEER with two highly efficient splatting-based methods that share similar processing stages: 3DGS on the MipNeRF360 dataset and FisheyeGS on the ScanNet++ dataset. As shown in Tab. 6, 3DGEER incurs

Table 6. **Runtime Analysis: Asso. Method on ScanNet++.** The efficiency of the PBF-based association is compared to the splatting-based EWA and UT with acceleration option SnugBox integrated into 3DGEER pipeline.

3DGEER Asso.	Prep.	Avg. Timings (ms) ↓				Avg. FPS ↑
		Dup.	Sort	Render	Total	
EWA	0.13	1.17	3.27	12.69	17.84	56
+ SnugBox	0.13	0.60	1.42	6.22	8.68	115
UT	0.13	0.71	1.94	7.97	11.16	90
+ SnugBox	0.13	0.28	0.64	3.16	4.38	228
PBF (Ours)	0.13	0.26	0.59	2.89	3.98	251

Table 7. **Impact of PBF-CSF Association.** The evaluation employs the artifact-sensitive LPIPS metric. To assess cross-model robustness, each variant is also tested using models trained with the other association strategies. Additionally, we report the performance gap between in-method and cross-method evaluations to quantify consistency and generalization.

Asso. Method	LPIPS ↓	Cross-LPIPS ↓	Δ LPIPS(1e-2) ↓
EWA	0.1250	0.1321	0.71
UT	0.1249	0.1302	0.53
PBF (Ours)	0.1245	0.1251	0.06

lower overhead in Gaussian duplication and sorting, offsetting the additional cost of ray-based rendering. As a result, it achieves overall runtime efficiency comparable to these optimized splatting methods.

Second, we evaluate the runtime of our ray-particle association strategy against projection-based alternatives—EWA [Zwicker et al. 2001] and UT [Wu et al. 2025]—within the 3DGEER framework. As shown in Tab. 6, our method consistently achieves a 2.5× to 5× speedup. This gain arises because projection-based schemes estimate screen-space bounds using first-order Taylor expansions or UT sampling, which often conservatively overestimate the extent using the maximum projected radius—leading to excessive overdraw and inefficient memory access in ray-based pipelines.

Even when accelerated with techniques like SnugBox [Hanson et al. 2025], projection-based methods remain fundamentally constrained by their reliance on approximated density centers. The resulting bounding regions are often misaligned with the true ray-projected distributions, leading to systematic inaccuracies (see Fig. 2). In fact, SnugBox can exacerbate these mismatches by tightening bounds around miscentered projections, further degrading visual fidelity, as shown in Fig. 8. Despite these refinements, such methods still fall short in speed compared to our approach.

5 ABLATION STUDIES

5.1 Impact of Particle Bounding Frustum (PBF).

We evaluate the effectiveness of the proposed PBF-based ray-particle association strategy under challenging large-FoV distortion settings using the ScanNet++ dataset. To quantify perceptual degradation, we adopt LPIPS [Zhang et al. 2018] as our primary metric, given its high sensitivity to structural and high-frequency artifacts—issues often overlooked by PSNR and SSIM. We compare our PBF-based association to two representative alternatives: the EWA-style 2D conic projection on the perspective image plane [Zwicker et al. 2001], and the Unscented Transform (UT) approximation [Wu et al.

Table 8. **Impact of BEAP.** The ablation compares BEAP against the Perspective representation derived from undistorted fisheye images, focusing on the central region using mask-weighted evaluation metrics.

Method	Supervision Space	Central Region	
		PSNR ↑	SSIM ↑
3DGS	Perspective	31.58	0.951
3DGEER w/o BEAP	Perspective	32.51	0.954
3DGEER (Default)	Angular	33.23	0.957

2025] in non-linear angular space. All methods are evaluated within the same 3DGEER training pipeline to ensure a modular and fair comparison.

As shown in Table 7, our PBF method achieves the lowest LPIPS, outperforming both projective and unscented approximations, which are more sensitive to projective distortion. In addition, we conduct cross-method evaluations by testing one method’s rendering using Gaussian fields trained under a different association scheme. This setup allows us to assess both cross-method robustness and method consistency. Our PBF method demonstrates significantly better generalization across these settings, indicating benefit of eliminating projective approximation errors at the association stage. These results also highlight 3DGEER’s potential as **an universal rendering method** that can improve novel view synthesis quality, even when applied to Gaussian fields reconstructed by other methods.

Qualitatively, Fig. 8 (Right) shows both projective and unscented bounding strategies exhibit aliasing and visibility artifacts, particularly at object boundaries and occlusions. Notably, similar artifacts are observed in the original 3DGUT implementation [Wu et al. 2025], as illustrated in Fig. 8 (Left). In contrast, our frustum-based association produces clean and artifact-free renderings—even when used with Gaussian fields trained under alternative bounding schemes.

5.2 Impact of Bipolar Equiangular Projection (BEAP)

We evaluate the effectiveness of BEAP by comparing it against standard perspective image representations within our 3DGEER pipeline, as well as the original 3DGS pipeline. To introduce a controlled level of challenge from large-FoV scenarios, we conduct experiments on rectified and centrally cropped images from ScanNet++ scenes, where fisheye images are undistorted into wide-FoV pinhole views. For fair comparison, all rendered outputs are reprojected into the native ScanNet++ coordinate space, and pixels falling outside the rectified FoV are masked during PSNR and SSIM evaluation. As shown in Table 8, BEAP—by supervising rays uniformly sampled in angular space—leads to significantly improved reconstruction fidelity over perspective-based sampling.

6 CONCLUSIONS

We presented 3DGEER, the first complete, closed-form solution for exact volumetric Gaussian rendering derived from first principles. To complement this formulation, we introduced an efficient PBF computation method for ray-particle association, enabling high-speed rendering while maintaining exactness. Additionally, we proposed the BEAP image representation to facilitate effective color supervision under wide-FoV camera models. Extensive experiments demonstrate that 3DGEER consistently outperforms state-of-the-art methods across multiple datasets, with particularly strong results in challenging wide-FoV scenarios.

REFERENCES

- Jonathan T. Barron, Ben Mildenhall, Matthew Tancik, Peter Hedman, Ricardo Martin-Brualla, and Pratul P. Srinivasan. 2021. Mip-NeRF: A Multiscale Representation for Anti-Aliasing Neural Radiance Fields. In *IEEE International Conference on Computer Vision (ICCV)*.
- Jonathan T. Barron, Ben Mildenhall, Dor Verbin, Pratul P. Srinivasan, and Peter Hedman. 2023. Zip-NeRF: Anti-Aliased Grid-Based Neural Radiance Fields. In *IEEE International Conference on Computer Vision, (ICCV)*.
- David Charatan, Sizhe Lester Li, Andrea Tagliasacchi, and Vincent Sitzmann. 2024. pixelsplat: 3d gaussian splats from image pairs for scalable generalizable 3d reconstruction. In *Proceedings of the IEEE/CVF conference on computer vision and pattern recognition (CVPR)*. 19457–19467.
- Yiwen Chen, Zilong Chen, Chi Zhang, Feng Wang, Xiaofeng Yang, Yikai Wang, Zhonggang Cai, Lei Yang, Huaping Liu, and Guosheng Lin. 2024a. Gaussianeditor: Swift and controllable 3d editing with gaussian splatting. In *Proceedings of the IEEE/CVF conference on computer vision and pattern recognition (CVPR)*. 21476–21485.
- Zilong Chen, Feng Wang, Yikai Wang, and Huaping Liu. 2024b. Text-to-3d using gaussian splatting. In *Proceedings of the IEEE/CVF conference on computer vision and pattern recognition (CVPR)*. 21401–21412.
- Kai Cheng, Xiaoxiao Long, Kaizhi Yang, Yao Yao, Wei Yin, Yuexin Ma, Wenping Wang, and Xuejin Chen. 2024. Gaussianpro: 3d gaussian splatting with progressive propagation. In *Forty-first International Conference on Machine Learning (ICML)*.
- Jaeyoung Chung, Jeongtaek Oh, and Kyoung Mu Lee. 2024. Depth-regularized optimization for 3d gaussian splatting in few-shot images. In *Proceedings of the IEEE/CVF Conference on Computer Vision and Pattern Recognition (CVPR)*. 811–820.
- Jorge Condor, Sébastien Speierer, Lukas Bode, Aljaz Bozic, Simon Green, Piotr Didyk, and Adrián Jarabo. 2025. Don't Splat your Gaussians: Volumetric Ray-Traced Primitives for Modeling and Rendering Scattering and Emissive Media. *ACM Trans. Graph.* (2025).
- Jonathan Courbon, Youcef Mezouar, Laurent Eckt, and Philippe Martinet. 2007. A generic fisheye camera model for robotic applications. In *IEEE/RSJ International Conference on Intelligent Robots and Systems, (IROS)*. 1683–1688.
- Daniel Duckworth, Peter Hedman, Christian Reiser, Peter Zhizhin, Jean-François Thibert, Mario Lucic, Richard Szeliski, and Jonathan T. Barron. 2024. SMERF: Streamable Memory Efficient Radiance Fields for Real-Time Large-Scene Exploration. *ACM Trans. Graph.* (2024).
- Antoine Guédon and Vincent Lepetit. 2024. Sugar: Surface-aligned gaussian splatting for efficient 3d mesh reconstruction and high-quality mesh rendering. In *Proceedings of the IEEE/CVF Conference on Computer Vision and Pattern Recognition (CVPR)*. 5354–5363.
- Yuliang Guo, Sparsh Garg, S. Mahdi H. Miangoleh, Xinyu Huang, and Liu Ren. 2025. Depth Any Camera: Zero-Shot Metric Depth Estimation from Any Camera. *Conference on Computer Vision and Pattern Recognition (CVPR)* (2025).
- Alex Hanson, Allen Tu, Geng Lin, Vasu Singla, Matthias Zwicker, and Tom Goldstein. 2025. Speedy-Splat: Fast 3D Gaussian Splatting with Sparse Pixels and Sparse Primitives. arXiv:2412.00578 [cs.CV] <https://arxiv.org/abs/2412.00578>
- Letian Huang, Jiayang Bai, Jie Guo, and Yanwen Guo. 2024. Gs++: Error analyzing and optimal gaussian splatting. *CoRR* (2024).
- Juho Kannala and Sami S Brandt. 2006. A generic camera model and calibration method for conventional, wide-angle, and fish-eye lenses. *IEEE transactions on pattern analysis and machine intelligence* (2006).
- Bernhard Kerbl, Georgios Kopanas, Thomas Leimkühler, and George Drettakis. 2023. 3D Gaussian Splatting for Real-Time Radiance Field Rendering. *ACM Trans. Graph.* (2023).
- Bernhard Kerbl, Andreas Meuleman, Georgios Kopanas, Michael Wimmer, Alexandre Lanvin, and George Drettakis. 2024. A hierarchical 3d gaussian representation for real-time rendering of very large datasets. *ACM Transactions on Graphics (TOG)* 43, 4 (2024), 1–15.
- Leonid Keselman and Martial Hebert. 2022. Approximate differentiable rendering with algebraic surfaces. In *European Conference on Computer Vision (ECCV)*.
- Shakiba Kheradmand, Daniel Rebain, Gopal Sharma, Weiwei Sun, Yang-Che Tseng, Hossam Isack, Abhishek Kar, Andrea Tagliasacchi, and Kwang Moo Yi. 2024. 3d gaussian splatting as markov chain monte carlo. *Advances in Neural Information Processing Systems (NeurIPS)* 37 (2024), 80965–80986.
- Varun Ravi Kumar, Ciarán Eising, Christian Witt, and Senthil Kumar Yogamani. 2023. Surround-view fisheye camera perception for automated driving: Overview, survey & challenges. *IEEE Transactions on Intelligent Transportation Systems* 24, 4 (2023), 3638–3659.
- Byeonghyeon Lee, Howoong Lee, Xiangyu Sun, Usman Ali, and Eunbyung Park. 2024a. Deblurring 3d gaussian splatting. In *European Conference on Computer Vision (ECCV)*. Springer, 127–143.
- Joo Chan Lee, Daniel Rho, Xiangyu Sun, Jong Hwan Ko, and Eunbyung Park. 2024b. Compact 3d gaussian representation for radiance field. In *Proceedings of the IEEE/CVF Conference on Computer Vision and Pattern Recognition (CVPR)*. 21719–21728.
- Zimu Liao, Siyan Chen, Rong Fu, Yi Wang, Zhongling Su, Hao Luo, Li Ma, Linning Xu, Bo Dai, Hengjie Li, et al. 2024. Fisheye-GS: Lightweight and Extensible Gaussian Splatting Module for Fisheye Cameras. *ECCV Workshop* (2024).
- Tao Lu, Mulin Yu, Linning Xu, Yuanbo Xiangli, Limin Wang, Dahua Lin, and Bo Dai. 2024. Scaffold-gs: Structured 3d gaussians for view-adaptive rendering. In *Proceedings of the IEEE/CVF Conference on Computer Vision and Pattern Recognition (CVPR)*. 20654–20664.
- Alexander Mai, Peter Hedman, George Kopanas, Dor Verbin, David Futschik, Qiang Xu, Falko Kuester, Jonathan T Barron, and Yinda Zhang. 2024. EVER: Exact Volumetric Ellipsoid Rendering for Real-time View Synthesis. *CoRR* (2024).
- Saswat Subhajiyo Mallick, Rahul Goel, Bernhard Kerbl, Markus Steinberger, Francisco Vicente Carrasco, and Fernando De La Torre. 2024. Taming 3dgs: High-quality radiance fields with limited resources. In *SIGGRAPH Asia 2024 Conference Papers*.
- Xiaoyang Mao, Lichan Hong, and Arie Kaufman. 1995. Splatting of curvilinear volumes. In *Proceedings Visualization '95*. IEEE, 61–68.
- Christopher Mei and Patrick Rives. 2007. Single view point omnidirectional camera calibration from planar grids. In *IEEE International Conference on Robotics and Automation. ICRA*.
- Nicolas Moëgne-Loccoz, Ashkan Mirzaei, Or Perel, Riccardo de Lutio, Janick Martinez Esturo, Gavriel State, Sanja Fidler, Nicholas Sharp, and Zan Gojic. 2024. 3D Gaussian Ray Tracing: Fast Tracing of Particle Scenes. *ACM Transactions on Graphics (TOG)* (2024).
- Nicolas Moëgne-Loccoz, Ashkan Mirzaei, Or Perel, Riccardo de Lutio, Janick Martinez Esturo, Gavriel State, Sanja Fidler, Nicholas Sharp, and Zan Gojic. 2024. 3D Gaussian Ray Tracing: Fast Tracing of Particle Scenes. *ACM Transactions on Graphics (TOG)* 43, 6 (2024), 1–19.
- Hazem Rashed, Eslam Mohamed, Ganesh Sistu, Varun Ravi Kumar, Ciaran Eising, Ahmad El-Sallab, and Senthil Yogamani. 2021. Generalized object detection on fisheye cameras for autonomous driving: Dataset, representations and baseline. In *Proceedings of the IEEE/CVF Winter Conference on Applications of Computer Vision, (WACV)*. 2272–2280.
- Samuel Rota Bulò, Lorenzo Porzi, and Peter Kotschieder. 2024. Revising densification in gaussian splatting. In *European Conference on Computer Vision (ECCV)*. Springer, 347–362.
- Johannes Lutz Schönberger and Jan-Michael Frahm. 2016. Structure-from-Motion Revisited. In *Conference on Computer Vision and Pattern Recognition (CVPR)*.
- Ahmed Rida Sekkat, Yohan Dupuis, Varun Ravi Kumar, Hazem Rashed, Senthil Yogamani, Pascal Vasseur, and Paul Honeine. 2022. SynWoodScape: Synthetic surround-view fisheye camera dataset for autonomous driving. *IEEE Robotics and Automation Letters* 7, 3 (2022), 8502–8509.
- Lee Westover. 1990. Footprint evaluation for volume rendering. In *Proceedings of the 17th annual conference on Computer graphics and interactive techniques*. 367–376.
- Qi Wu, Janick Martinez Esturo, Ashkan Mirzaei, Nicolas Moëgne-Loccoz, and Zan Gojic. 2025. 3DGUT: Enabling Distorted Cameras and Secondary Rays in Gaussian Splatting. *Conference on Computer Vision and Pattern Recognition (CVPR)* (2025).
- Zhiwen Yan, Weng Fei Low, Yu Chen, and Gim Hee Lee. 2024. Multi-scale 3d gaussian splatting for anti-aliased rendering. In *Proceedings of the IEEE/CVF Conference on Computer Vision and Pattern Recognition, (CVPR)*. 20923–20931.
- Chandan Yeshwanth, Yueh-Cheng Liu, Matthias Nießner, and Angela Dai. 2023. ScanNet++: A high-fidelity dataset of 3d indoor scenes. In *Proceedings of the IEEE/CVF International Conference on Computer Vision*.
- Senthil Yogamani, Ciarán Hughes, Jonathan Horgan, Ganesh Sistu, Padraig Varley, Derek O'Dea, Michal Uricár, Stefan Milz, Martin Simon, Karl Amende, et al. 2019. Woodscape: A multi-task, multi-camera fisheye dataset for autonomous driving. In *Proceedings of the IEEE/CVF International Conference on Computer Vision (ICCV)*. 9308–9318.
- Senthil Yogamani, David Unger, Venkatraman Narayanan, and Varun Ravi Kumar. 2024. FisheyeBEVSeg: Surround View Fisheye Cameras based Bird's-eye View Segmentation for Autonomous Driving. In *Proceedings of the IEEE/CVF Conference on Computer Vision and Pattern Recognition, (CVPR)*. 1331–1334.
- Zehao Yu, Anpei Chen, Binbin Huang, Torsten Sattler, and Andreas Geiger. 2024a. Mip-splatting: Alias-free 3d gaussian splatting. In *Proceedings of the IEEE/CVF conference on computer vision and pattern recognition, (CVPR)*. 19447–19456.
- Zehao Yu, Torsten Sattler, and Andreas Geiger. 2024b. Gaussian Opacity Fields: Efficient Adaptive Surface Reconstruction in Unbounded Scenes. *ACM Transactions on Graphics* (2024).
- Richard Zhang, Phillip Isola, Alexei A Efros, Eli Shechtman, and Oliver Wang. 2018. The unreasonable effectiveness of deep features as a perceptual metric. In *Proceedings of the IEEE conference on computer vision and pattern recognition (CVPR)*. 586–595.
- Zheng Zhang, Wenbo Hu, Yixing Lao, Tong He, and Hengshuang Zhao. 2024. Pixel-gs: Density control with pixel-aware gradient for 3d gaussian splatting. In *European Conference on Computer Vision (ECCV)*. Springer, 326–342.
- Zichao Zhang, Henri Rebecq, Christian Forster, and Davide Scaramuzza. 2016. Benefit of large field-of-view cameras for visual odometry. In *2016 IEEE International Conference on Robotics and Automation (ICRA)*. IEEE, 801–808.
- Matthias Zwicker, Hanspeter Pfister, Jeroen Van Baar, and Markus Gross. 2001. EWA volume splatting. In *Proceedings Visualization, 2001. VIS'01*. IEEE, 29–538.

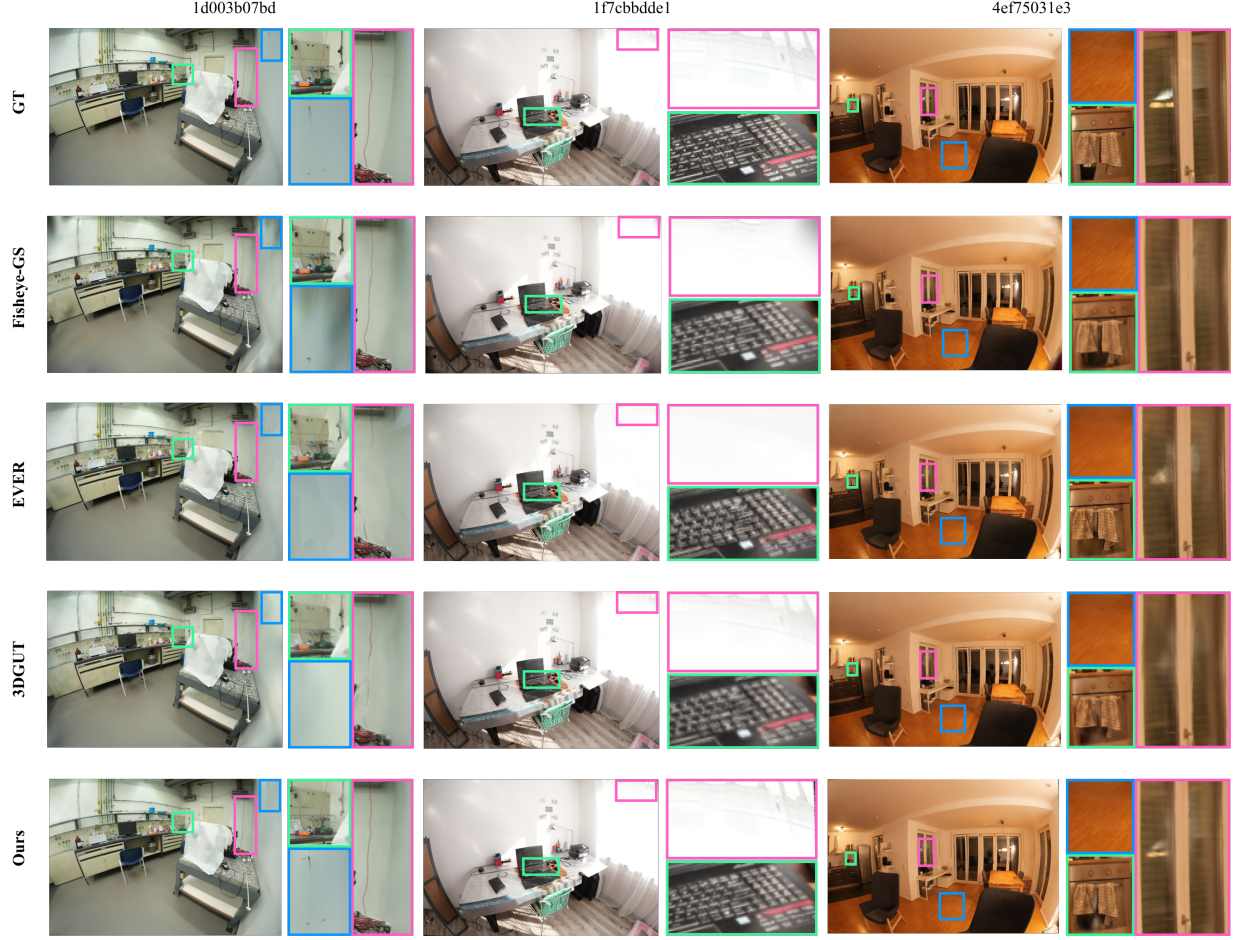


Fig. 7. **Qualitative Results on the ScanNet++ Dataset.** Larger differences are visible in the zoomed-in colored boxes, particularly in structural details and artifact regions. Our method demonstrates superior reconstruction fidelity and stronger resistance to rendering artifacts compared to previous methods.

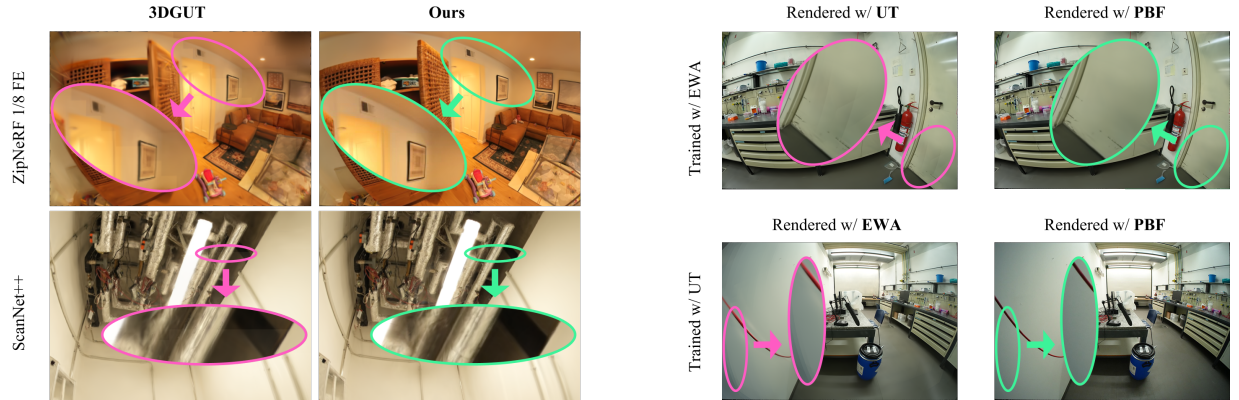


Fig. 8. **Visual Impact of 3DGEER on Artifacts and Cross-Method Robustness.** *Left:* Rendering comparisons on ZipNeRF-FE and ScanNet++ datasets. Notable artifacts appear in 3DGUT due to imprecise tile-to-AABB associations under distorted camera models, while our 3DGEER produces clean, artifact-free renderings. *Right:* Our PBF-CSF association demonstrates superior cross-method robustness compared to prior association strategies. **Pink** highlights regions rendered by prior methods; **Green** indicates corresponding regions rendered by our 3DGEER or corrected using PBF-CSF.

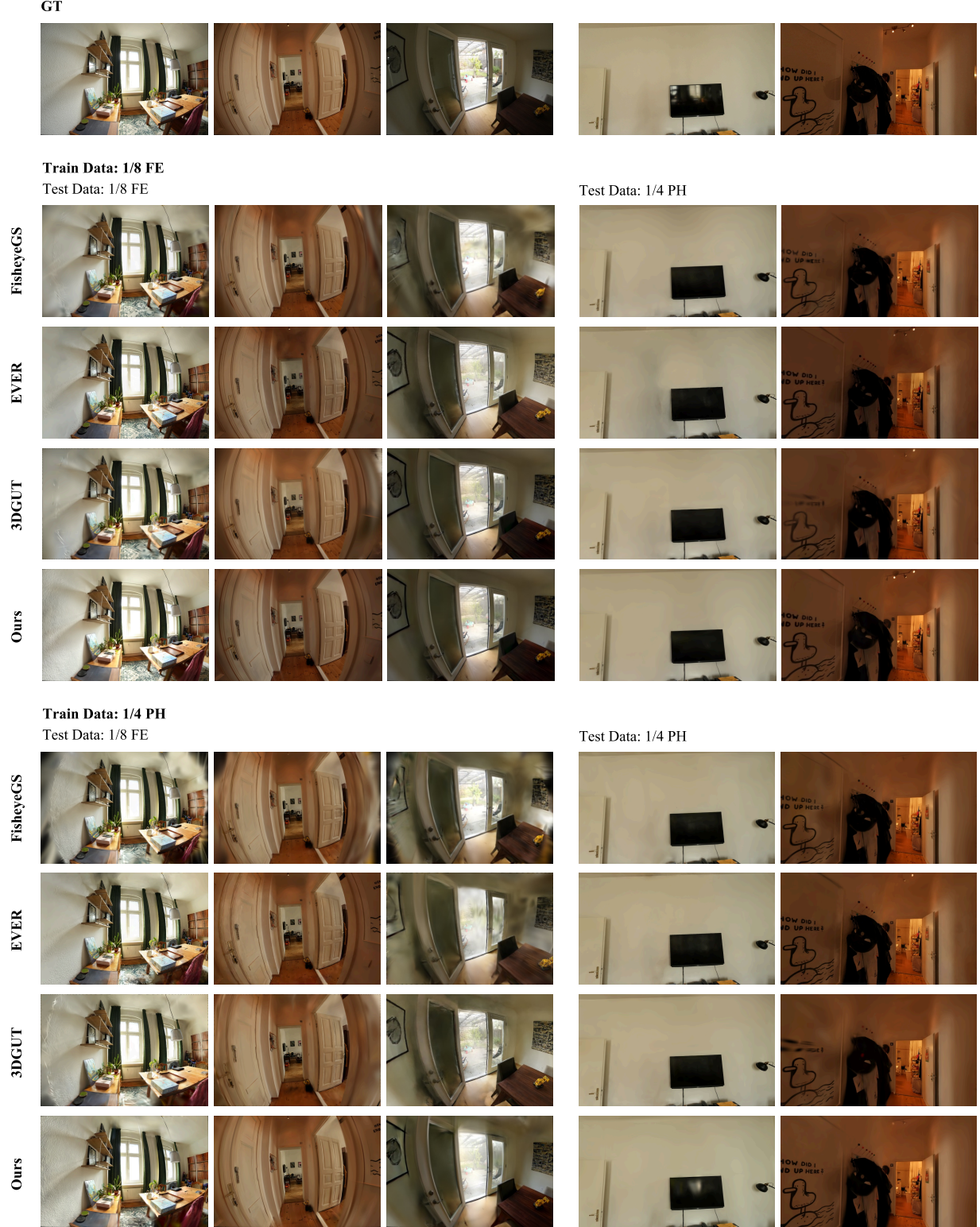


Fig. 9. **Qualitative Results on the ZipNeRF Dataset with Cross-Camera Generalization.** Performance differences are more pronounced in peripheral regions of Fisheye (FE) results and in the most challenging Pinhole (PH) train – Fisheye test setup, where our method demonstrates a significant advantage.

A EXTENDED VISUAL EXPLANATIONS

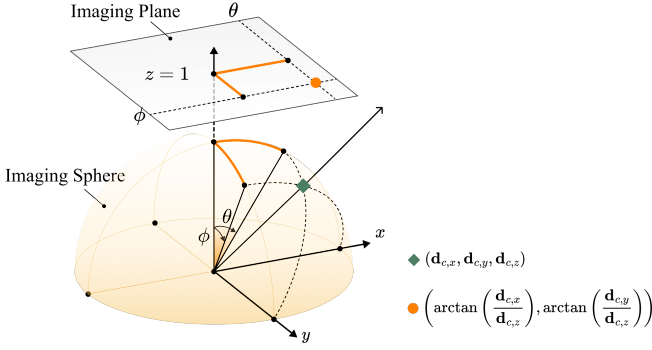


Fig. A.1. **An Illustration of the Two Spherical Angles Defining PBF and BEAP.** A view-space direction \mathbf{d}_c is first normalized onto the optical sphere (green spade), followed by angular projections onto the xz and yz planes. The orange point denotes the resulting coordinate (θ, ϕ) on the unfolded BEAP imaging plane.

B MATHEMATICAL PROOF TO RAY-GAUSSIAN TRANSMITTANCE IN CANONICAL SPACE

THEOREM B.1 (RAY INTEGRAL OF ISOTROPIC 3D GAUSSIAN). *Given a ray and a standard isotropic 3D Gaussian, the ray-Gaussian integral has a closed-form proportional to:*

$$\exp\left(-\frac{1}{2}D^2\right),$$

where D is the perpendicular distance from the Gaussian center to the ray.

PROOF. We first apply a translation to the coordinate system such that the Gaussian \mathcal{G} is centered at the origin, and the ray \mathbf{r}_u is translated accordingly. Next, we rotate the entire scene so that the ray direction is aligned with the z -axis. Due to the translation-invariance of the integral and the isotropy of the standard Gaussian, these transformations do not affect the result of the integral. The translated standard isotropic 3D Gaussian is defined as:

$$\mathcal{G}_{1,0}(\mathbf{u}) = \frac{1}{\rho} \exp\left(-\frac{1}{2}\mathbf{u}^\top \mathbf{u}\right), \quad (\text{B.1})$$

which matches Eq. 6. Let the z -axis aligned ray as:

$$\mathbf{r}_u(t) = \begin{bmatrix} \mathbf{o}_u \\ \mathbf{o}_v \\ 0 \end{bmatrix} + t \begin{bmatrix} 0 \\ 0 \\ 1 \end{bmatrix}, \quad (\text{B.2})$$

the ray-Gaussian integral becomes:

$$\begin{aligned} \int_{t \in \mathbb{R}} \mathcal{G}_{1,0}(\mathbf{r}_u(t)) dt &= \frac{1}{\rho} \exp\left(-\frac{u_0^2 + v_0^2}{2}\right) \int_{t \in \mathbb{R}} \exp\left(-\frac{1}{2}t^2\right) dt \\ &= \frac{\sqrt{2\pi}}{\rho} \exp\left(-\frac{1}{2}D^2\right), \end{aligned} \quad (\text{B.3})$$

where $D^2 = \frac{u_0^2 + v_0^2}{2}$ denotes the squared perpendicular distance from the ray to the Gaussian center in canonical space. Thus, the integral is proportional to $\exp\left(-\frac{1}{2}D^2\right)$, as stated in theorem. \square

Note that the density function shared by our 3D primitives in the canonical space (see Eq. 6) follows the same formulation as in the isotropic case. Given the world-coordinate ray (\mathbf{o}, \mathbf{d}) as the input of D , its value also depends on the world-space Gaussian parameters $\boldsymbol{\mu}, \Sigma$, which are used to transform the ray into the canonical coordinate system. Therefore, for each Gaussian contributing to the ray, we derive the transmittance as:

$$T = \frac{\sqrt{2\pi}\sigma}{\rho} \exp\left(-\frac{1}{2}(D_{\boldsymbol{\mu}, \Sigma}(\mathbf{o}, \mathbf{d}))^2\right), \quad (\text{B.4})$$

which recovers Eq. 7 when $\rho = \sqrt{2\pi}$.

C COOKBOOK OF GRADIENT COMPUTATION

C.1 Chain Rule

Recall that $T = \sigma\alpha$ is the ray-Gaussian transmittance (Eq. 7), where σ is the opacity coefficient, and α is the ray-Gaussian integral. We denote $\kappa = D_{\boldsymbol{\mu}, \Sigma}^2$ as the minimal squared Mahalanobis distance from the ray to the Gaussian distribution, S as the Gaussian scaling, and R as the rotation matrix in the world space. Additionally, given $\Sigma = RSS^\top R^\top$ as the 3D covariance matrix of the Gaussian in the world space, we have W_{pca} as the PCA whitening matrix satisfying:

$$W_{\text{pca}} = \Sigma^{-\frac{1}{2}} = S^{-1}R^\top, \quad (\text{C.1})$$

$$\text{where } S^{-1} = \text{diag}\left(\frac{1}{s}\right).$$

As illustrated in Figure 4, we can apply the chain rule to find derivatives w.r.t. the Gaussian parameters, e.g. scaling vector \mathbf{s} , rotation quaternion \mathbf{q} , and mean $\boldsymbol{\mu}$:

$$\frac{\partial T}{\partial \mathbf{s}} = \frac{\partial T}{\partial \kappa} \frac{\partial \kappa}{\partial W_{\text{pca}}} \frac{\partial W_{\text{pca}}}{\partial \mathbf{s}}, \quad (\text{C.2})$$

$$\frac{\partial T}{\partial \mathbf{q}} = \frac{\partial T}{\partial \kappa} \frac{\partial \kappa}{\partial W_{\text{pca}}} \frac{\partial W_{\text{pca}}}{\partial \mathbf{q}}, \quad (\text{C.3})$$

$$\frac{\partial T}{\partial \boldsymbol{\mu}} = \frac{\partial T}{\partial \kappa} \frac{\partial \kappa}{\partial \boldsymbol{\mu}}. \quad (\text{C.4})$$

C.2 Two-Stage Propagation

To reduce computational overhead in shared propagation, we design our gradient computation following the structured two-stage approach of 3DGS [Kerbl et al. 2023], comprising RenderCUDA (RC) and PreprocessCUDA (PC). The former performs ray-wise accumulation, efficiently accelerated by our Particle Bounding Frustum (PBF) association (See section 3.3), while the latter operates with Gaussian-wise complexity, leveraging view frustum culling for additional speedup.

According to Eq. 7, we can respectively write the gradient w.r.t. opacity coefficient and the shared partial derivative for Gaussian parameters in RC as:

$$\left. \frac{\partial T}{\partial \sigma} \right|_{\text{RC}} = \alpha, \quad \left. \frac{\partial T}{\partial \kappa} \right|_{\text{RC}} = -\frac{T}{2}. \quad (\text{C.5})$$

The remaining gradients to the Gaussian parameters can then be back-propagated from the squared distance, e.g., $\frac{\partial \kappa}{\partial \mathbf{s}}, \frac{\partial \kappa}{\partial \mathbf{q}}, \frac{\partial \kappa}{\partial \boldsymbol{\mu}}$.

C.3 Gradients for Canonical Ray

We then backpropagate gradients to the canonical ray parameters: the origin \mathbf{o}_u , direction \mathbf{d}_u , and moment $\mathbf{m}_u = \mathbf{o}_u \times \mathbf{d}_u$, as defined in Eq. 8 in our paper. These quantities directly influence the Mahalanobis distance in Eq. 9 and are critical for capturing canonical ray geometry.

$$\left. \frac{\partial \kappa}{\partial \mathbf{m}_u} \right|_{\text{RC}} = \left(\frac{2}{\mathbf{d}_u^\top \mathbf{d}_u} \right) \mathbf{m}_u, \quad (\text{C.6})$$

$$\left. \frac{\partial \kappa}{\partial \mathbf{o}_u} \right|_{\text{RC}} = \frac{\partial \kappa}{\partial \mathbf{m}_u} \times \mathbf{d}_u, \quad (\text{C.7})$$

$$\left. \frac{\partial \kappa}{\partial \mathbf{d}_u} \right|_{\text{RC}} = - \left(\frac{2\kappa}{\mathbf{d}_u^\top \mathbf{d}_u} \right) \mathbf{d}_u + \mathbf{o}_u \times \frac{\partial \kappa}{\partial \mathbf{m}_u}. \quad (\text{C.8})$$

C.4 Gradients for Whitening Matrix

Recall that $\mathbf{d}_u = W_{\text{pca}} \mathbf{d}$ and $\mathbf{o}_u = W_{\text{pca}}(\mathbf{o} - \boldsymbol{\mu})$, where $\mathbf{o} = -R_c^\top \mathbf{t}_c$ denotes the world space optical center, and \mathbf{d} denotes the ray direction. Once the gradients *w.r.t.* the ray parameters are obtained, we further propagate them to the PCA whitening matrix W_{pca} via outer products with the world-space vectors:

$$\begin{aligned} \text{RenderCUDA: } \left. \frac{\partial \kappa}{\partial W_{\text{pca}}} \right|_{\text{RC}} &= \frac{\partial \kappa}{\partial \mathbf{d}_u} \mathbf{d}^\top; \\ \text{PreprocessCUDA: } \left. \frac{\partial \kappa}{\partial W_{\text{pca}}} \right|_{\text{PC}} &= \frac{\partial \kappa}{\partial \mathbf{o}_u} (\mathbf{o} - \boldsymbol{\mu})^\top; \\ \text{Overall: } \left. \frac{\partial \kappa}{\partial W_{\text{pca}}} \right| &= \left. \frac{\partial \kappa}{\partial W_{\text{pca}}} \right|_{\text{RC}} + \left. \frac{\partial \kappa}{\partial W_{\text{pca}}} \right|_{\text{PC}}. \end{aligned} \quad (\text{C.9})$$

Here, the gradient backpropagated through \mathbf{d}_u is accumulated ray-wise in RenderCUDA, while the gradient through \mathbf{o}_u is computed Gaussian-wise in PreprocessCUDA. These two components are then summed to yield the complete gradient *w.r.t.* the PCA transformation matrix W_{pca} .

C.5 Gradients for Scaling and Rotation

Thus, for scaling gradients $\frac{\partial \kappa}{\partial \mathbf{s}} = \frac{\partial \kappa}{\partial W_{\text{pca}}} \frac{\partial W_{\text{pca}}}{\partial \mathbf{s}}$, we have:

$$\left. \frac{\partial W_{\text{pca}}^{i,j}}{\partial s_k} \right|_{\text{PC}} = \begin{cases} -\frac{1}{s_k^2} R_{j,k} & \text{if } i = k \\ 0 & \text{otherwise} \end{cases}. \quad (\text{C.10})$$

To derive gradients for rotation $\frac{\partial \kappa}{\partial \mathbf{q}} = \frac{\partial \kappa}{\partial W_{\text{pca}}} \frac{\partial W_{\text{pca}}}{\partial \mathbf{q}}$, given the quaternion form $\mathbf{q} = q_r + q_i \mathbf{i} + q_j \mathbf{j} + q_k \mathbf{k}$, we can write the whitening matrix as:

$$W_{\text{pca}} = 2 \begin{pmatrix} \frac{1}{s_1} (\frac{1}{2} - q_j^2 - q_k^2) & \frac{1}{s_1} (q_i q_j + q_r q_k) & \frac{1}{s_1} (q_i q_k - q_r q_j) \\ \frac{1}{s_2} (q_i q_j - q_r q_k) & \frac{1}{s_2} (\frac{1}{2} - q_i^2 - q_k^2) & \frac{1}{s_2} (q_j q_k + q_r q_i) \\ \frac{1}{s_3} (q_i q_k + q_r q_j) & \frac{1}{s_3} (q_j q_k - q_r q_i) & \frac{1}{s_3} (\frac{1}{2} - q_i^2 - q_j^2) \end{pmatrix}. \quad (\text{C.11})$$

As a result, we derive the following end gradients for the quaternion \mathbf{q} as:

$$\begin{aligned} \left. \frac{\partial W_{\text{pca}}}{\partial q_r} \right|_{\text{PC}} &= 2 \begin{pmatrix} 0 & \frac{q_k}{s_1} & -\frac{q_j}{s_1} \\ -\frac{q_k}{s_2} & 0 & \frac{q_i}{s_2} \\ \frac{q_j}{s_3} & -\frac{q_i}{s_3} & 0 \end{pmatrix}, \quad \left. \frac{\partial W_{\text{pca}}}{\partial q_i} \right|_{\text{PC}} = 2 \begin{pmatrix} 0 & \frac{q_j}{s_1} & \frac{q_k}{s_1} \\ \frac{q_j}{s_2} & -\frac{2q_i}{s_2} & \frac{q_r}{s_2} \\ \frac{q_k}{s_3} & -\frac{q_r}{s_3} & -\frac{2q_i}{s_3} \end{pmatrix}, \\ \left. \frac{\partial W_{\text{pca}}}{\partial q_j} \right|_{\text{PC}} &= 2 \begin{pmatrix} -\frac{2q_k}{s_1} & \frac{q_i}{s_1} & -\frac{q_r}{s_1} \\ \frac{q_i}{s_2} & 0 & \frac{q_k}{s_2} \\ \frac{q_r}{s_3} & \frac{q_k}{s_3} & -\frac{2q_j}{s_3} \end{pmatrix}, \quad \left. \frac{\partial W_{\text{pca}}}{\partial q_k} \right|_{\text{PC}} = 2 \begin{pmatrix} -\frac{2q_k}{s_1} & \frac{q_r}{s_1} & \frac{q_i}{s_1} \\ -\frac{q_r}{s_2} & -\frac{2q_k}{s_2} & \frac{q_j}{s_2} \\ \frac{q_i}{s_3} & \frac{q_j}{s_3} & 0 \end{pmatrix}. \end{aligned} \quad (\text{C.12})$$

C.6 Gradients for 3D Mean

Meanwhile, we compute end gradients *w.r.t.* the Gaussian 3D mean $\boldsymbol{\mu}$ as:

$$\left. \frac{\partial \kappa}{\partial \boldsymbol{\mu}} \right|_{\text{PC}} = -W_{\text{pca}}^\top \frac{\partial \kappa}{\partial \mathbf{o}_u}. \quad (\text{C.13})$$

D HIGH-LEVEL ALGORITHMIC SUMMARY

We provide a high-level overview of our volumetric rendering pipeline (See Alg. 1 and Alg. 2). For clarity, we follow the structure of 3DGS [Kerbl et al. 2023] to illustrate differences: newly introduced modules or replaced ones are highlighted in **green**, and significantly modified ones in **yellow**.

ALGORITHM 1: GPU Software Asso. & Render.

Function 3DGEER($\boldsymbol{\mu}, \mathbf{s}, \mathbf{q}, c, \sigma, \mathbf{r}_c, V$):

- CullGaussian($\boldsymbol{\mu}, V$) ▷ Frustum Culling
- $F \leftarrow \text{InitCSFs}(\mathbf{w}, h, K)$ ▷ **Partition**
- $\Sigma_c, \boldsymbol{\mu}_c \leftarrow \text{ViewspaceGaussians}(\mathbf{s}, \mathbf{q}, V)$ ▷ **Transform**
- $F_{ID} \leftarrow \text{PBF_Intersect}(\Sigma_c, \boldsymbol{\mu}, F)$ ▷ **Sub-frustum Asso.**
- $W_{\text{pca}} \leftarrow \text{PCA_Whitening}(\mathbf{s}, \mathbf{q})$ ▷ **Transform**
- $\mathcal{G}_{ID}, F_K \leftarrow \text{DuplicateWithKeys}(W_{\text{pca}}, F_{ID})$ ▷ **Indices (Gaussian) & Keys (FrustumID+Depth)**
- $\text{SortByKey}(\mathcal{G}_{ID}, F_K)$ ▷ Globally Depth Sort
- $R \leftarrow \text{IdentifyFrustumRanges}(F, F_K)$
- $I \leftarrow 0$ ▷ **Init Canvas (w/ Rays)**
- for all** CSFs $f \leftarrow I$ **do**
- for all** Rays $i \leftarrow f$ **do**
- $r \leftarrow \text{GetFrustumRange}(R, f)$
- $\mathbf{m}_u, \mathbf{d}_u \leftarrow \text{Cano_Ray}(W_{\text{pca}}, \boldsymbol{\mu}, i)$ ▷ **Transform**
- $D_{\boldsymbol{\mu}, \Sigma} \leftarrow \text{Dist}(\mathbf{m}_u, \mathbf{d}_u)$ ▷ **Mah-distance**
- $I[i] \leftarrow \text{BlendInOrder}(i, \mathcal{G}_{ID}, r, F_K, D_{\boldsymbol{\mu}, \Sigma}, c, \sigma)$ ▷ Alpha Blending
- end**
- end**
- return** I

E ADDITIONAL DETAILS IN ASSOCIATION

E.1 Particle Bounding Frustum (PBF) Solver

Recall Eq. 12, we define $P = (VH)^\top \in \mathbb{R}^{4 \times 4}$ as the plane transformation matrix from the view space to the canonical space. Take the unknown bounds for $c = \tan \theta_{1,2}$ as example, we have:

$$\mathbf{g}_u = -P_0 + cP_2 = \begin{bmatrix} -P_{00} + cP_{02} \\ -P_{10} + cP_{12} \\ -P_{20} + cP_{22} \\ -P_{30} + cP_{32} \end{bmatrix}, \quad (\text{E.1})$$

ALGORITHM 2: 3DGEER Initialization and Training Framework
 w, h : width and height of the training images
 K, V : intrinsics and extrinsic meta info.

```

    ▶ Init Gaussian Attributes
     $\mu \leftarrow \text{SfM Points}$                                 ▶ Position
     $s, q \leftarrow \text{InitAttributes}()$                     ▶ Scaling, Rotation
     $c, \sigma \leftarrow \text{InitCoefficients}()$               ▶ Color, Opacity
    while not converged do
         $r_c, \hat{C} \leftarrow \text{BEAP}(w, h, K)$                 ▶ View Rays / Colors
        ▶ Asso. & Render
         $C \leftarrow 3\text{DGEER}(\mu, s, q, c, \sigma, r_c, V)$     ▶ See Alg. 1
         $\mathcal{L} \leftarrow \text{Loss}(C, \hat{C})$                         ▶ Loss
         $\mu, s, q, c, \sigma \leftarrow \text{Adam}(\nabla \mathcal{L})$         ▶ Backprop & Step
        if IsRefinementIteration( $i$ ) then
             $\mu, s, q, c, \sigma \leftarrow \text{Optimize}(\mu, s, q, c, \sigma)$  ▶ [Kerbl et al. 2023]
        end
    end
end

```

where P_i denotes i -th row of the matrix, expressed as a 4×1 column vector, and P_{ij} further denotes j -th element. Recall Eq. 13, assuming we are computing the bounding box of the 1-standard-deviation contour ellipsoid of the Gaussian, i.e., $\lambda = 1$, then we have the following quadratic equation:

$$((f \circ P_2^T) \cdot P_2) c^2 - 2((f \circ P_0^T) \cdot P_2) c + (f \circ P_0^T) \cdot P_0 = 0, \quad (\text{E.2})$$

where $f = (1, 1, 1, -1)$ is a 1×4 row vector. Here we denote the equation as:

$$\mathcal{T}_{22}c^2 - 2\mathcal{T}_{02}c + \mathcal{T}_{00} = 0, \quad (\text{E.3})$$

where \mathcal{T} is a 3×3 upper triangular matrix defined with $\mathcal{T}_{ij} = (f \circ P_i^T) \cdot P_j$.

Similarly, for the bounds of ϕ , we have $c = \tan \phi_{1,2}$ satisfying:

$$\mathcal{T}_{22}c^2 - 2\mathcal{T}_{12}c + \mathcal{T}_{11} = 0. \quad (\text{E.4})$$

Interestingly, given a camera-view configuration $[R_c \mid t_c]$, we find that the parameter matrix \mathcal{T} can be efficiently computed from the Gaussian's view-space covariance $\Sigma_c = R_c R S S^T R^T R_c^T$ and 3D mean $\mu_c = R_c \mu + t_c$:

$$\mathcal{T}_{ij} = \lambda^2 \Sigma_c^{i,j} - (\mu_c \mu_c^T)^{i,j}. \quad (\text{E.5})$$

Thus, we can compute the angular bounds (defined by their tangent-space center and extent) from:

$$\begin{aligned} \left(\frac{\tan \theta_1 + \tan \theta_2}{2}, \frac{\tan \phi_1 + \tan \phi_2}{2} \right) &= \left(\frac{\mathcal{T}_{02}}{\mathcal{T}_{22}}, \frac{\mathcal{T}_{12}}{\mathcal{T}_{22}} \right), \\ \|\tan \theta_1 - \tan \theta_2\| &= \frac{2\sqrt{\mathcal{T}_{02}^2 - \mathcal{T}_{22}\mathcal{T}_{00}}}{|\mathcal{T}_{22}|}, \\ \|\tan \phi_1 - \tan \phi_2\| &= \frac{2\sqrt{\mathcal{T}_{12}^2 - \mathcal{T}_{22}\mathcal{T}_{11}}}{|\mathcal{T}_{22}|}. \end{aligned} \quad (\text{E.6})$$

If the discriminant of either quadratic is negative—indicating that the camera's optical center lies inside the Gaussian ellipsoid and the angular bounds are undefined—we conservatively clamp the frustum angles using the camera's maximum field of view (FoV).

Note that this result is directly computed from the 3D view-space true covariance, in contrast to methods like EWA and UT, which

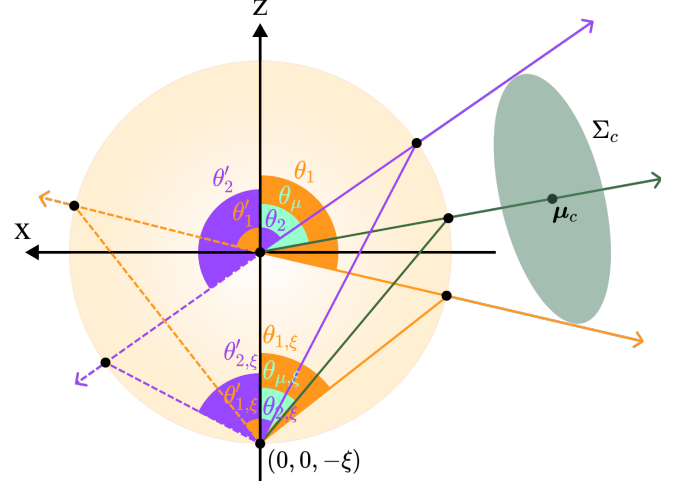


Fig. E.1. Mirror Transformation of PBF Angular Bounds. Four candidate mirrored angles $\theta_{1,\xi}, \theta'_{1,\xi}, \theta_{2,\xi}, \theta'_{2,\xi}$ are generated from a given pair of bounds. Given a Gaussian centered at μ_c , the two closest to the corresponding Gaussian's mirrored angle $\theta_{\mu,\xi}$ are used as PBF bounds for robust intersection with mirror-transformed CSF partitions.

rely on intermediate conic approximations in screen space. Our PBF formulation offers both exactness and efficiency.

E.2 Details in Computing CSF-PBF Intersection

We uniformly sample spherical angles within the maximum field of view (FoV). The resulting x , y , and z coordinates—i.e., the ray direction vectors \mathbf{d} —are projected onto a unit sphere and then transformed into pixel space for inverse color interpolation (see Appendix F). These sampled rays are then grouped according to their corresponding CSFs for subsequent Gaussian association.

In most scenes using a pinhole camera with a limited FoV, the angular bounds in PBF typically lie within $[-\frac{\pi}{2}, \frac{\pi}{2}]$. In such cases, since the tan function is monotonically increasing over this interval, the intersections between PBF and CSFs can be computed by directly comparing the tan values of their respective angular bounds. However, in wide FoV scenarios, even when the incidence angle formed by the Gaussian centers remains within $[-\frac{\pi}{2}, \frac{\pi}{2}]$, the angular bounds used in PBF may still fall outside the monotonic region of the tan function. In these cases, directly comparing tan values may yield incorrect PBF-CSF intersections, such as mistakenly matching angular bounds as $[\theta'_2, \theta_1]$ (see Figure E.1 for an example).

To resolve the correct intersections, we introduce a mirror transformation applied to the tangent values of both PBF angular bounds and CSF partitions. Inspired by the CMEI camera model [Mei and Rives 2007], we shift the optical center using a mirror parameter ξ , leading to the following transformation:

$$\tan \theta_\xi = \frac{\tan \theta}{1 + \xi \frac{z}{\|z\|}} = \frac{\sin \theta}{\cos \theta + \xi}, \quad (\text{E.7})$$

where θ_ξ represents the mirror-transformed angle of θ on the xz -plane, using a mirror parameter ξ . We set $\xi = 1$ throughout all experiments.

Given a pair of tangent value $[\tan \theta_1, \tan \theta_2]$ from our PBF solver (See Equation. E.6), this transformation yields four candidate mirror angles, as illustrated in Figure E.1. The Gaussian center, in contrast, corresponds to a unique mirror-transformed angle $\theta_{\mu, \xi}$. We exploit this property by selecting the two candidate angles closest to $\theta_{\mu, \xi}$. These two then define the effective lower and upper bounds for PBF, i.e., $[\theta_{1, \xi}, \theta_{2, \xi}]$, which are subsequently compared with CSF partitions to compute the correct intersections.

This trick ensures robust and consistent angular comparisons, even beyond the monotonic domain of the tan function. As reported in our timing analysis (Table 6), the pre-processing pipeline—including the mirror-angle-based PBF-CSF intersection computation and the canonical transformation for all Gaussians—takes less than 0.13 ms in total. This confirms the efficiency of our approach, even when applied to thousands of Gaussians across wide FoV scenarios.

F BEAP IMAGE INVERSE INTERPOLATION

To prepare training data, we sample rays to comprehensively cover the original image FoVs and use them as input to our CUDA renderer. Simultaneously, we interpolate the ground truth color for each input ray to ensure accurate and uniform supervision during training.

The projection of sampled rays onto observed images begins with transforming the incidence angle projections θ and ϕ into normalized ray direction vectors $\mathbf{d} = (x, y, z)^\top$, expressed as:

$$x = \frac{\sin \theta \cos \phi}{\sqrt{\sin^2 \theta \cos^2 \phi + \cos^2 \theta \sin^2 \phi + \cos^2 \theta \cos^2 \phi}}, \quad (\text{F.1})$$

$$y = \frac{\cos \theta \sin \phi}{\sqrt{\sin^2 \theta \cos^2 \phi + \cos^2 \theta \sin^2 \phi + \cos^2 \theta \cos^2 \phi}}, \quad (\text{F.2})$$

$$z = \frac{\cos \theta \cos \phi}{\sqrt{\sin^2 \theta \cos^2 \phi + \cos^2 \theta \sin^2 \phi + \cos^2 \theta \cos^2 \phi}}. \quad (\text{F.3})$$

Several camera models are provided to subsequently project the normalized rays $(x, y, z)^\top$ into pixel space $(x_p, y_p, 1)^\top$.

Pinhole Camera Model. For pinhole camera models, we first have $\frac{x}{z} = \tan \theta$ and $\frac{y}{z} = \tan \phi$. Thus, we have:

$$\begin{bmatrix} x_p \\ y_p \\ 1 \end{bmatrix} = \begin{bmatrix} f_x & 0 & c_x \\ 0 & f_y & c_y \\ 0 & 0 & 1 \end{bmatrix} \begin{bmatrix} \tan \theta \\ \tan \phi \\ 1 \end{bmatrix}. \quad (\text{F.4})$$

KB Fisheye Model. We have the incidence angle φ derived from its projections:

$$r = \sqrt{\tan^2 \theta + \tan^2 \phi} \quad \text{and} \quad \varphi = \arctan(r). \quad (\text{F.5})$$

And we have the fisheye distorted angle:

$$\varphi_d = \varphi(1 + k_1 \varphi^2 + k_2 \varphi^4 + k_3 \varphi^6 + k_4 \varphi^8). \quad (\text{F.6})$$

As a result, the rays are projected onto pixel space, allowing for inverse color interpolation from:

$$\begin{bmatrix} x_p \\ y_p \\ 1 \end{bmatrix} = \begin{bmatrix} \frac{f_x \varphi_d}{r} & 0 & c_x \\ 0 & \frac{f_y \varphi_d}{r} & c_y \\ 0 & 0 & 1 \end{bmatrix} \begin{bmatrix} \tan \theta \\ \tan \phi \\ 1 \end{bmatrix}. \quad (\text{F.7})$$

G ADDITIONAL IMPLEMENTATION DETAILS

Central and peripheral regions in ScanNet++ evaluation. The rays sampled in the central part follows the range:

$$\theta \in [-\frac{w}{2f_x}, \frac{w}{2f_x}], \phi \in [-\frac{h}{2f_y}, \frac{h}{2f_y}].$$

And the Peripheral part takes the rays sampled in remaining angle ranges. Here w, h indicate the width and height of the image and f_x, f_y are the focal lengths defined in the original KB camera model. **Cross-camera generalization evaluation on ZipNeRF.** ZipNeRF provides two sets of data: fisheye raw images and their corresponding undistorted frames, which are generated by applying distortion correction and cropping the central regions. Although the frames are aligned on a per-frame basis, camera poses and point clouds were independently reconstructed using COLMAP [Schönberger and Frahm 2016] for each set. Due to COLMAP’s global optimization independently refining camera trajectories, applying a single rigid transformation to align the two pose sets is insufficient and may introduce alignment errors. To ensure reliable cross-camera evaluation without introducing errors from structure-from-motion (SfM), we always use the same set of test-time camera poses as those used during training. In cross-camera experiments, we vary only the intrinsic parameters, while keeping the extrinsic poses fixed. This ensures fair comparisons without entangling pose inconsistencies arising from preprocessing.

H ADDITIONAL RESULTS

See Next Page for *Full Experiment Results*.

I EWA SPLATTING PRELIMINARIES - LOCAL APPROXIMATION ERROR

From camera coordinates to ray coordinates As the coordinate definitions in EWA Splatting [Zwicker et al. 2001], we have the following mapping function from the camera (view) space points \mathbf{t} to the ray space points \mathbf{x} for projective transformation in pinhole camera models, i.e., $\tau: \mathbf{t} \xrightarrow{\sim} \mathbf{x}$:

$$\mathbf{x} = \begin{bmatrix} x_0 \\ x_1 \\ x_2 \end{bmatrix} = \tau(\mathbf{t}) = \begin{bmatrix} t_0/t_2 \\ t_1/t_2 \\ \|(t_0, t_1, t_2)^\top\| \end{bmatrix}, \quad (\text{I.1})$$

$$\mathbf{t} = \begin{bmatrix} t_0 \\ t_1 \\ t_2 \end{bmatrix} = \tau^{-1}(\mathbf{x}) = \begin{bmatrix} x_0/l \cdot x_2 \\ x_1/l \cdot x_2 \\ 1/l \cdot x_2 \end{bmatrix}, \quad (\text{I.2})$$

$$, \text{ where } l = \|(x_0, x_1, 1)^\top\|. \quad (\text{I.3})$$

These mappings are not affine, which requires computationally expensive [Mao et al. 1995; Westover 1990] or locally approximated solutions [Kerbl et al. 2023; Zwicker et al. 2001] to calculate integral in the ray space.

Local affine approximation EWA splatting by Zwicker et al. [2001] introduced local affine approximation, denoted as τ_k , to keep the linear effects and the k -indexed reconstruction kernels as Gaussians in 2D screen space. It is defined by the first two terms of the Taylor expansion of τ at the camera space point \mathbf{t}_k , then the ray

Table H.1. **ScanNet++ Quantitative Results by Sequence (Full FoV)**. The overall results are shown in Tab. 2.

Method	0a5c013435			2a1a3afad9			1f7cbbdde1			4ef75031e3			1d003b07bd		
	PSNR ↑	SSIM ↑	LPIPS ↓	PSNR ↑	SSIM ↑	LPIPS ↓	PSNR ↑	SSIM ↑	LPIPS ↓	PSNR ↑	SSIM ↑	LPIPS ↓	PSNR ↑	SSIM ↑	LPIPS ↓
EVER	28.24	0.916	0.164	27.80	0.899	0.169	32.60	0.948	0.131	29.77	0.924	0.213	28.96	0.936	0.156
FisheyeGS	24.74	0.932	0.146	25.75	0.927	0.145	31.95	0.970	0.095	29.72	0.944	0.177	26.91	0.959	0.129
3DGUT	29.26	0.934	0.147	29.37	0.928	0.145	34.65	0.967	0.112	30.78	0.941	0.196	29.12	0.948	0.151
Ours	29.18	0.940	0.141	29.78	0.935	0.125	34.94	0.974	0.084	31.17	0.946	0.168	32.43	0.968	0.114

Table H.2. **ZipNeRF Quantitative Results by Sequence**. Alameda, Berlin, London, and NYC in order. The overall results are shown in Tab. 3.

Train Data Test Data Method	1/8 FE		1/8 FE		1/8 FE		1/4 PH		1/4 PH		1/4 PH	
	1/8 FE	1/4 PH	1/8 FE	1/4 PH	1/8 FE	1/4 PH	1/8 FE	1/4 PH	1/8 FE	1/4 PH	1/8 FE	1/4 PH
	PSNR ↑	SSIM ↑	PSNR ↑	SSIM ↑	PSNR ↑	SSIM ↑	PSNR ↑	SSIM ↑	PSNR ↑	SSIM ↑	PSNR ↑	SSIM ↑
FisheyeGS	20.74	23.64	0.820	0.802	0.223	0.277	17.39	23.74	0.736	0.839	0.265	0.240
EVER	22.46	23.06	0.852	0.777	0.144	0.274	20.06	22.83	0.789	0.794	0.213	0.250
3DGUT	21.78	22.39	0.841	0.718	0.193	0.368	17.03	22.58	0.588	0.765	0.329	0.311
Ours	24.60	25.00	0.857	0.839	0.154	0.241	21.49	25.21	0.792	0.807	0.232	0.277

Train Data Test Data Method	1/8 FE		1/8 FE		1/8 FE		1/4 PH		1/4 PH		1/4 PH	
	1/8 FE	1/4 PH	1/8 FE	1/4 PH	1/8 FE	1/4 PH	1/8 FE	1/4 PH	1/8 FE	1/4 PH	1/8 FE	1/4 PH
	PSNR ↑	SSIM ↑	PSNR ↑	SSIM ↑	PSNR ↑	SSIM ↑	PSNR ↑	SSIM ↑	PSNR ↑	SSIM ↑	PSNR ↑	SSIM ↑
FisheyeGS	24.25	28.25	0.895	0.924	0.206	0.209	20.08	27.86	0.848	0.929	0.233	0.194
EVER	25.26	26.97	0.912	0.907	0.155	0.221	23.18	27.72	0.877	0.913	0.196	0.212
3DGUT	25.37	27.02	0.904	0.876	0.197	0.288	18.57	27.43	0.730	0.898	0.297	0.249
Ours	25.51	29.15	0.916	0.925	0.166	0.194	23.58	29.51	0.878	0.915	0.219	0.228

Train Data Test Data Method	1/8 FE		1/8 FE		1/8 FE		1/4 PH		1/4 PH		1/4 PH	
	1/8 FE	1/4 PH	1/8 FE	1/4 PH	1/8 FE	1/4 PH	1/8 FE	1/4 PH	1/8 FE	1/4 PH	1/8 FE	1/4 PH
	PSNR ↑	SSIM ↑	PSNR ↑	SSIM ↑	PSNR ↑	SSIM ↑	PSNR ↑	SSIM ↑	PSNR ↑	SSIM ↑	PSNR ↑	SSIM ↑
FisheyeGS	23.57	26.65	0.829	0.861	0.253	0.254	20.83	27.33	0.768	0.883	0.288	0.229
EVER	24.59	26.83	0.823	0.859	0.218	0.223	23.14	26.98	0.793	0.860	0.268	0.235
3DGUT	25.61	26.25	0.854	0.803	0.221	0.336	19.82	26.41	0.669	0.833	0.313	0.291
Ours	26.60	27.84	0.895	0.882	0.142	0.230	23.95	27.15	0.840	0.846	0.217	0.289

Train Data Test Data Method	1/8 FE		1/8 FE		1/8 FE		1/4 PH		1/4 PH		1/4 PH	
	1/8 FE	1/4 PH	1/8 FE	1/4 PH	1/8 FE	1/4 PH	1/8 FE	1/4 PH	1/8 FE	1/4 PH	1/8 FE	1/4 PH
	PSNR ↑	SSIM ↑	PSNR ↑	SSIM ↑	PSNR ↑	SSIM ↑	PSNR ↑	SSIM ↑	PSNR ↑	SSIM ↑	PSNR ↑	SSIM ↑
FisheyeGS	24.15	27.21	0.890	0.885	0.162	0.215	19.41	27.50	0.811	0.907	0.203	0.183
EVER	28.39	27.71	0.931	0.860	0.095	0.228	25.22	28.27	0.879	0.883	0.154	0.192
3DGUT	26.31	26.69	0.917	0.817	0.121	0.302	19.00	27.42	0.659	0.866	0.263	0.228
Ours	28.26	28.49	0.922	0.906	0.097	0.190	24.52	28.55	0.874	0.885	0.168	0.220

Table H.3. **MipNeRF360 Quantitative Results by Sequence**. The overall results are shown in Tab. 4.

Method	Metric	Bicycle	Bonsai	Counter	Garden	Kitchen	Stump	Flowers	Room	Treehill
Ours	PSNR↑	25.63	32.23	29.05	27.60	31.78	26.83	21.83	32.09	22.83
	SSIM↑	0.774	0.946	0.910	0.860	0.931	0.774	0.613	0.946	0.637
	LPIPS↓	0.223	0.175	0.195	0.136	0.120	0.246	0.340	0.108	0.344

space point \mathbf{x} near around \mathbf{x}_k can be estimated by:

$$\mathbf{x} = \tau(\mathbf{t}) = \mathbf{x}_k + \mathbf{J}_\tau^{\mathbf{t}_k}(\mathbf{t} - \mathbf{t}_k), \quad (\text{I.4})$$

where $\mathbf{J}_\tau^{\mathbf{t}_k}$ is the Jacobian matrix given by the partial derivatives of τ at the point \mathbf{t}_k . For the k -indexed 3D Gaussian $\mathcal{G}_{\Sigma, \mu}$ in a certain camera coordinate, using EWA local affine transformation, the approximated density function can be expressed as a 3D Gaussian $\mathcal{G}_{\Sigma_k, \mathbf{x}_k}$ in the ray coordinate. For $\forall \mathbf{x}$ around \mathbf{x}_k , we have:

$$\mathcal{G}_{\Sigma_k, \mathbf{x}_k}(\mathbf{x}) = \frac{1}{(2\pi)^{\frac{3}{2}} |\Sigma_k|^{\frac{1}{2}}} \exp\left(-\frac{1}{2}(\mathbf{x} - \mathbf{x}_k)^\top \Sigma_k^{-1}(\mathbf{x} - \mathbf{x}_k)\right), \quad (\text{I.5})$$

$$\text{where } \Sigma_k = \mathbf{J}_\tau^{\mathbf{t}_k} \Sigma \left(\mathbf{J}_\tau^{\mathbf{t}_k}\right)^\top. \quad (\text{I.6})$$

Integrating a 3D Gaussian $\mathcal{G}_{\Sigma_k, \mathbf{x}_k}^{(3)}$ along one coordinate axis yields a 2D Gaussian $\mathcal{G}_{\hat{\Sigma}_k, \hat{\mathbf{x}}_k}^{(2)}$, hence:

$$\int_{\mathbb{R}} \mathcal{G}_{\Sigma_k, \mathbf{x}_k}^{(3)}(\mathbf{x}) dx_2 = \mathcal{G}_{\hat{\Sigma}_k, \hat{\mathbf{x}}_k}^{(2)}(\hat{\mathbf{x}}), \quad (\text{I.7})$$

where $\hat{\mathbf{x}} = \begin{bmatrix} x_0 \\ x_1 \end{bmatrix}$, and the mean $\hat{\mathbf{x}}_k = \begin{bmatrix} x_{k,0} \\ x_{k,1} \end{bmatrix}$, and the 2×2 variance matrix $\hat{\Sigma}_k$ is easily obtained from the 3×3 matrix Σ_k by skipping the third row and column.

Splatting approximation error Although we can not expect the density function in ray space still obey the Gaussian distribution when we apply general projective transformation to the original view space, exact density can be derived through substitution via

Eq. I.2:

$$\begin{aligned}\mathcal{G}_{\Sigma, \mu}(\mathbf{t}) &= \mathcal{G}_{\Sigma, \mu}(\tau^{-1}(\mathbf{x})) \\ &= \frac{1}{(2\pi)^{\frac{3}{2}} |\Sigma_k|^{\frac{1}{2}}} \exp\left(-\frac{1}{2} \left(\tau^{-1}(\mathbf{x}) - \mathbf{t}_k\right)^\top \Sigma_k^{-1} \left(\tau^{-1}(\mathbf{x}) - \mathbf{t}_k\right)\right),\end{aligned}\tag{I.8}$$

which means that the approximation error can be estimated through Monte Carlo integration of the following equation:

$$\mathcal{E}_k = \int_{\mathbb{R}} \left| \mathcal{G}_{\Sigma, \mu}(\tau^{-1}(\mathbf{x})) - \mathcal{G}_{\Sigma_k, \mathbf{x}_k}(\mathbf{x}) \right| dx_2. \tag{I.9}$$

Note that x_2 represents the dimension along the ray direction in the ray coordinate.